# **Evaluating Weather and Chemical Transport Models at High Latitudes using MAGIC2021 Airborne Measurements**

Félix Langot<sup>1</sup>, Cyril Crevoisier<sup>1</sup>, Thomas Lauvaux<sup>2</sup>, Charbel Abdallah<sup>2</sup>, Jérôme Pernin<sup>1</sup>, Xin Lin<sup>3</sup>, Marielle Saunois<sup>3</sup>, Axel Guedj<sup>1</sup>, Thomas Ponthieu<sup>1</sup>, Julien Moyé<sup>3</sup>, Michel Ramonet<sup>3</sup>, Anke Roiger<sup>4</sup>, Klaus-Dirk Gottschaldt<sup>4</sup>, and Alina Fiehn<sup>4</sup>

**Abstract.** High latitude wetland emissions of methane  $(CH_4)$  remain a significant source of uncertainty in global methane budgets. At these latitudes, flux estimation approaches, such as atmospheric inversions, are challenged by complex meteorological conditions, limited observational coverage, and uncertainties in atmospheric transport modelling. This study evaluates the performance of various atmospheric transport models and reanalysis datasets using meteorological and CH<sub>4</sub> in-situ measurements collected during the MAGIC2021 campaign near Kiruna, Sweden. Over six days of measurements in August 2021, the ERA5 reanalysis, produced by the European Centre for Medium-Range Weather Forecasts (ECMWF) and providing global atmospheric data, showed better agreement with observations compared to the meso-scale Weather Research and Forecasting (WRF) model, though WRF provided valuable insights into local atmospheric dynamics. Among global simulations of CH<sub>4</sub> mixing ratios, inversion-optimised models which adjust emissions to match observations, achieved the best performance overall particularly when constrained by surface measurements. Regional simulations from WRF coupled with chemistry (WRF-Chem) revealed biases in CH<sub>4</sub> mixing ratios in the boundary layer, suggesting an overestimation of emissions by wetland models. All chemistry-transport models exhibited a positive bias in the stratosphere. Simulations with higher vertical resolution demonstrated an improved representation of vertical CH<sub>4</sub> profiles in the upper layers of the atmosphere. Despite its limited spatio-temporal coverage, we were able to identify the best performing transport models and to evaluate fluxes from different biogeochemical model parameterisations using the MAGIC2021 high-resolution dataset, demonstrating the utility of in-situ vertical profile datasets for transport and flux model evaluation.

## 1 Introduction

In recent years, the Earth's climate has been rapidly changing, with significant impacts on polar and sub-polar regions. In the Arctic, the rate of warming was thought to be around twice as fast as the global average until recently (AMAP, 2021; Jansen et al., 2020; Walsh, 2014; Yu et al., 2021), but it is now estimated to be closer to 4 times faster (Rantanen et al.,

<sup>&</sup>lt;sup>1</sup>Laboratoire de Météorologie Dynamique (LMD/IPSL), CNRS, Ecole Polytechnique, 91128 Palaiseau Cedex, France <sup>2</sup>Groupe de Spectrométrie Moléculaire et Atmopshérique (GSMA), CNRS, Université de Reims-Champagne-Ardenne (URCA), 51100, Reims, France

<sup>&</sup>lt;sup>3</sup>Laboratoire des Sciences du Climat et de l'Environnement (LSCE/IPSL), CEA/CNRS, L'Orme des Merisiers, Paris-Saclay, 91191 Gif-sur-Yvette Cedex, France

<sup>&</sup>lt;sup>4</sup>Deutsches Zentrum für Luft- und Raumfahrt (DLR), Institut für Physik der Atmosphäre, Oberpfaffenhofen, Germany **Correspondence:** Félix Langot (felix.langot@lmd.ipsl.fr)

2022). The amount of greenhouse gas in the atmosphere and the meteorological conditions are essential components of the circumpolar climate system, where positive climate feedback loops are ubiquitous and disruptive (boreal fires (Zheng et al., 2023), permafrost (Miner et al., 2022; MacDougall, 2021), wetland emissions(Zhang et al., 2023), and albedo (Hall, 2004; Booth et al., 2024)). However, a scarcity of long-term direct observational data in the region has proven to be a challenge for studies aiming to constrain uncertainties and changes in the regional methane cycle (Wittig et al., 2023). In order to understand these changes, climate models are therefore highly relied upon, and direct measurements must be employed to provide an assessment of their performance in modelling mixing ratios of greenhouse gases in the region.

In-situ data at high latitudes mainly come from several surface measurement networks operated by Arctic countries, as depicted in Wittig et al. (2023). In Europe, data collection is coordinated by the Integrated Carbon Observation System (ICOS) network, which comprises several towers stationed in Fennoscandia (few above the polar circle), that measure either in-situ atmospheric mixing ratios or methane fluxes through eddy covariance. mixing ratios are however only measured close to the surface. They are mostly representative of local scales and lack vertical information. Measurements covering larger scales and higher atmospheric layers are crucial for accurately modelling the regional methane budget. Several projects have carried out field measurements of atmospheric methane at high latitudes recently, including campaigns from the NASA ABoVE initiative (Sweeney et al., 2022) or the NASA-ESA joint initiative Arctic Methane and Permafrost Challenge (AMPAC, Miller et al. (2021)). This latest project was notably involved in the CoMet 2.0 Arctic campaign set in Canada and Alaska in 2022 (DLR, 2022), and MAGIC2021, set near Kiruna, Sweden (67 °N). The study presented here focuses on MAGIC2021 (Crevoisier, 2021), which spanned from 14 to 27 August 2021 and included airborne measurements of meteorological variables and atmospheric methane mixing ratios, combined with weather data sounding. The Monitoring Atmospheric composition and Greenhouse gases through multi-Instruments Campaigns (MAGIC) initiative launched by Centre National de la Recherche Scientifique (CNRS) and Centre Nationale des Études Spatiales (CNES) aims at improving knowledge of CO<sub>2</sub> and CH<sub>4</sub> distribution and emissions in the Earth's atmosphere by organising frequent measurement campaigns in different regions of interest. The first three campaigns, set in France from 2018 to 2020, served as a mean to calibrate and validate instruments and measurement techniques, whilst also validating current space missions. MAGIC2021 was therefore the first MAGIC campaign to focus on the study of CH<sub>4</sub> emissions at high latitudes, bringing together 70 participants from 17 teams and 7 different countries. As field work is relatively recent, few results have been published yet and, to our knowledge, no study has tried to extensively assess atmospheric composition models using campaign data at high resolution in those regions.

Kiruna and its surrounding area are characterised by wetland landscapes that include small ponds to large lakes as well as peatland and various inundated soils found in both boreal forest and tundra ecosystems, as shown on the left panel of Figure 1, where land cover comes from European Environment Agency (2019). These wetlands are known to be the main local source of methane though their emissions are generally poorly constrained (Saunois et al., 2020). Additionally, some permafrost areas are also present at higher altitudes found in the Scandinavian mountains west of the city, though to a relatively small extent (Ahlenius, 2016). In lower parts of the atmosphere, model estimates of greenhouse gas mixing ratios can be strongly affected by these high uncertainties in emission processes, particularly for methane. Boundary layer mixing ratios are also strongly influenced by turbulent flow which is parametrised in global models and challenging to simulate accurately at finer

scale (Schuh et al., 2019). This has a strong influence on atmospheric composition at all levels, as CH<sub>4</sub> released at the surface is usually transported to deeper atmospheric levels via turbulent and/or convective fine scale processes. Above the boundary layer, transport by geostrophic wind becomes the major driver for greenhouse gas mixing ratios. This means that atmospheric methane content is no longer strongly dependent on local emissions, but rather influenced by medium to long range transport. Stohl (2004) have shown that mixing ratios observed in Northern Europe can be traced back to emissions from North America or Siberia, provided meteorological conditions allowed for transport of surface emissions to the free troposphere. At higher altitudes, an important driver of CH<sub>4</sub> mixing ratios becomes methane depletion by OH radicals and other molecules (e.g. Cl, Li et al. (2018)). Their presence mostly affect methane mixing ratios in the upper troposphere and lower stratosphere, where stratification and reaction with these chemical species reduce drastically CH<sub>4</sub> mixing ratios in the upper troposphere and above the tropopause. Upper-tropospheric and lower-stratospheric CH<sub>4</sub> mixing ratios are therefore characterised by a strong vertical gradient. Tropopause height and troposphere/stratosphere exchanges are thus key influences on CH<sub>4</sub> mixing ratios (Xiong et al., 2013), and are also challenging to model accurately (Mateus et al., 2022).

In this study, the accuracy and precision of several models in reproducing greenhouse gas mixing ratios and meteorological conditions observed at fine scale are assessed. Our study uses in-situ observations that employed research aircraft and weather balloons deployed around Kiruna in August 2021 (details in Section 2). We first start by assessing models regarding meteorological variables, with data from the European Centre for Medium-Range Weather Forecasts (ECMWF) fifth-generation reanalysis (ERA5) global product and regional WRF simulations. Then, we assess the atmospheric composition models ability to reproduce observed CH<sub>4</sub> mixing ratios. Models assessed include the Copernicus Atmosphere Monitoring Service (CAMS) analysis *hlkx* and inversion-optimised flux product version 21r1, six PYVAR-LMDz-SACS ensemble inversions and WRF-Chem regional simulations. More detail about these models can be found in Section 2. Comparisons between model simulations and observational data provide insights into the strengths and limitations of these models in the Lapland region and highlight areas for improvement at several levels and scales.

## 2 Methods

## 2.1 Observational data

Both ground-based and airborne measurements were taken during MAGIC2021. This study focuses on airborne data taken by CNES weather balloons as well as two aeroplanes, an ATR42 from SAFIRE and a Cessna from *Deutsches Zentrum für Luft-und Raumfahrt* (DLR). These platforms had different payload configurations and measurement capabilities and thus provide complementary information about the distribution of gases in the atmosphere. Whilst this study does not make use of the full set of MAGIC2021 measurements due to data availability at the time of our analysis, it provides a solid example of such campaigns capability in terms of model validation. All data were put on the WMO scale (Hall et al., 2021) through several inter-comparisons and inter-calibrations using similar gas tanks on each Picarro analysers. These were carried out during the campaign, and included a wing-by-wing flight by the ATR42 and Cessna aircraft.

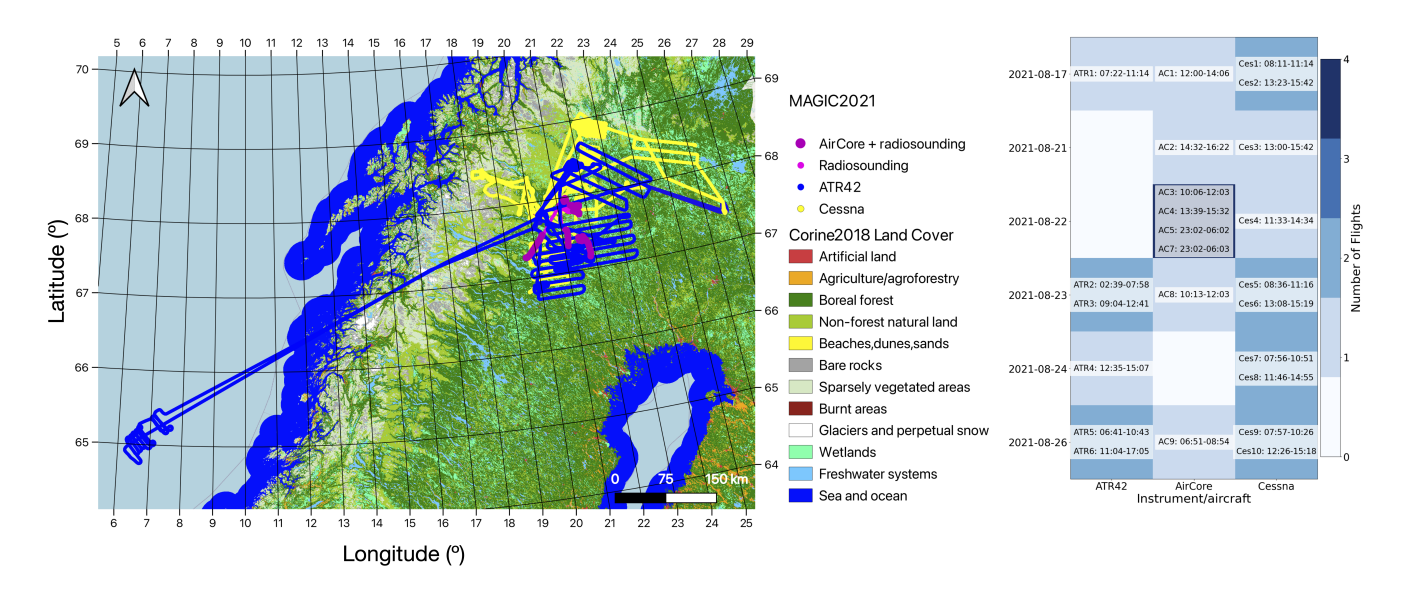


**Figure 1.** Location (left) and date and time (right) of MAGIC2021 measurements used in this study. Map background shows land use adapted from the Corine2018 dataset (European Environment Agency, 2019). Individual land cover types from the Corine2018 dataset are grouped in broader categories to ease map interpretation. Notably, wetlands include inland marshes, peat bogs, salt marshes, salines, intertidal flats, coastal lagoons and estuaries, i.e. both freshwater and saltwater wetlands.

#### 2.1.1 Weather balloon observations

100

Two types of weather balloons from CNES were released during MAGIC2021: the Light Inflatable Balloon (BLD - *Ballon Léger Dilatable*) and the Zero Pressure Difference (ZPD) balloon. Balloon types differ in their usage, BLD are single-use, their membrane bursting after the ascent phase. They typically reach altitudes up to 30km. ZPD are reusable and can reach altitudes above 30km. Weather balloons carried two main instruments whose data were used in the study: the AirCore atmospheric sampler, and meteomodem M20 radiosondes. The M20 instrument is an ultra-lightweight (36 grams) radiosonde used to gather meteorological data such as temperature, humidity, pressure, as well as zonal (U) and meridional (V) wind components. More details about the instrument can be found at Meteomodem (2020). Measurements with the M20 were made during both ascending and descending phases of balloon flights.

AirCore is an atmospheric sampler (Tans, 2009; Karion et al., 2010; Membrive et al., 2017) which allows sampling atmospheric composition on a large range of altitudes (~0 - 30km) making use of the atmospheric pressure gradient. To be more specific, the AirCore is made of a coated stainless steel tube that is filled with a calibration gas before release. The length of that tube varies according to the AirCore type: light AirCores have a shorter tube than high resolution AirCores. The sampler is then attached to a weather balloon that is released from the surface. During the ascending phase, the relatively high pressure inside the tube pushes out the calibration gas. At the top of the trajectory, the balloon pops and the payload starts a descending phase during which increasing pressure outside of the tube pushes atmospheric air inside the AirCore. Similarly to ice cores, the

resulting sample consists of a continuous profile of atmospheric air, with the most recently sampled air (from lower altitudes) located near the inlet and the earlier sampled air (from higher altitudes) located deeper within the tube. Both light AirCore and high resolution AirCore were deployed during MAGIC2021. After sampling, AirCores were retrieved and analysed on the ground, using the G2401 instrument from Picarro<sup>©</sup> (Picarro, 2008) which measured CH<sub>4</sub>, CO<sub>2</sub>, and H<sub>2</sub>O. Time and trajectories of measurements for the AirCore instrument are shown in Figure 1. Atmospheric composition observations used in this study include 8 separate weather balloon soundings. For meteorological data, only 6 of the 8 weather balloons were used due to radiosondes malfunctioning during two of the flights, but meteorological data were acquired during both ascent and descent flight phases which allowed to compensate for missing data.

# 2.1.2 Aircraft observations

110

120

125

130

Two research aircraft flew between the surface and approximately 8 km, carrying instruments that gathered atmospheric composition and weather data: the SAFIRE ATR 42-320 (CNES, CNRS, Météo France), abbreviated as ATR42, and the DLR Cessna C-208B Grand Caravan, abbreviated as Cessna. The position, velocity, and altitude of the ATR42 aircraft were recorded by both an iXBlue<sup>TM</sup> inertial reference/navigation system called SAFIRE AIRINS and a NovAtel<sup>TM</sup> Global Positioning System (GPS). This GPS system consists of L1/L2 GPS-Antennae (5x) and a OEM3 receiver. Water vapour and relative humidity were measured using a non dew/frost point hygrometer called SAFIRE relative humidity sensor, made by Michell Instruments<sup>TM</sup>. Airspeed, incidence angle and turbulence were measured by a Rosemount & Sextant<sup>TM</sup> incident flow vector probe called SAFIRE five hole radome. This instrument allows the measurement of U and V wind components. Finally, the Rosemount<sup>TM</sup> in-situ temperature sensor called SAFIRE Rosemount PT102E2AL, measures the temperature at the aircraft's location. Also on board the ATR42 were two Picarro<sup>TM</sup> models previously mentioned that were used for in-situ atmospheric composition analysis, as well as several other instruments distributed on the aircraft that gathered meteorological data.

The Cessna aircraft was equipped with a system called blackMAMBA (Measurement Acquisition of Meteorological Basics) that delivered track (i.e. position and time) data, together with aircraft status and meteorological parameters. Some of the meteorological sensors were installed in the MetPod, a container with a nose boom, mounted under the left wing. This allows atmospheric parameters to be measured with less distortion than if they were measured from the fuselage. The temperature, pressure, humidity sensors and the calibration of the wind measurement system are described in detail by (Mallaun et al., 2015). The aircraft also carried two in-situ trace gas instruments. Here we use only the data from a Picarro G1301m, which measured CH<sub>4</sub>, CO<sub>2</sub>, and H<sub>2</sub>O mixing ratios. More details about gas measurements can be found in Fiehn et al. (2020).

Observations used in this study include 6 ATR42 and 10 Cessna flights for both atmospheric composition and meteorological data.

## 2.2 Atmospheric modelling systems

This section describes model data that was compared to MAGIC2021 observations. The first two sections describe global models whilst the third focuses on the regional modelling system based on WRF-Chem that was specifically set up for MAGIC2021.

# 2.2.1 Global meteorological reanalysis

Global meteorological fields used in this study came from the European Centre for Medium-Range Weather Forecasts (ECMWF) fifth-generation reanalysis product (ERA5, Hersbach et al. (2020); C3S (2018)), that provides meteorological data on a global scale from 1950 to present. In our study, we assessed ERA5 reanalysis wind, temperature, and humidity. The high density of vertical levels in ERA5 from the mid-troposphere down to ground level allows for accurate comparison with the flights from MAGIC2021. Our analysis was carried out using ERA5 at time resolution of 1 hour, spatial resolution of 0.25° and 137 vertical levels. Horizontal ERA5 wind was given in terms of zonal (U) and meridional (V) components of the wind vector. Both observations and model data were converted to horizontal wind speed V and direction  $\theta$  for comparison when needed using:  $V = \sqrt{U^2 + V^2}$ ;  $\theta = \tan^{-1}(-U, -V) \cdot \frac{180}{\pi}$  (Tetzner et. al 2019). To compare humidity from models (given as specific humidity q in ERA5) to measured relative humidity (RH), ERA5 data was converted to RH using RH =  $\frac{e}{e_s}$  where e is the partial pressure of water vapour in air (pressure exerted by water molecules) and  $e_s$  is the saturation vapour pressure, or the maximum vapour pressure achievable at a given temperature before condensation occurs.

# 2.2.2 Global CH<sub>4</sub> assimilation systems

145

150

160

165

The Copernicus Atmosphere Monitoring Service (CAMS) is a service provided by ECMWF. Its atmospheric composition product combines satellite data and ground-based measurements in a 4D-Var assimilation system to provide comprehensive information on key atmospheric parameters such as mixing ratios of greenhouse gases in 4 dimensions (Peuch et al., 2022). Two CAMS products are used in this study. The first is the CAMS *hlkx* analysis (Agustí-Panareda et al., 2023) which is based on ECMWF Integrated Forecast System for Composition (C-IFS, Verma et al. (2017)), with a vertical resolution of 137 vertical levels, a horizontal resolution of 0.25° and 6 hours of temporal resolution. Methane loss to OH in the upper troposphere and stratosphere is provided by Bergamaschi et al. (2009) where CH<sub>4</sub> destruction was simulated using OH fields based on methyl chloroform optimised Carbon Bond Mechanism 4 (CBM-4) chemistry (Bergamaschi et al., 2005; Houweling et al., 1998). Non-OH stratospheric loss is based on the 2-D photochemical MaxPlanck-Institute (MPI) model (Brühl and Crutzen, 1993).

The second CAMS product compared to MAGIC2021 is the global inversion-optimised greenhouse gas mixing ratios product for CH<sub>4</sub> version 21r1 (Segers, 2023). This product makes use of methane mixing ratio measurements from the NOAA ground observations network to optimise a priori fluxes of CH<sub>4</sub> and produce 3D mixing ratios and correspond better to ground observations. Simulations are run using the chemistry transport model TM5-MP (Williams et al., 2017) that includes upper tropospheric and stratospheric computation of CH<sub>4</sub> loss using monthly mixing ratios of sink tracers, built-in reaction rates and monthly temperature estimates. Tropospheric or stratospheric reaction rates are attributed using a latitude dependent tropopause parameterisation from Lawrence et al. (2001). The spatial resolution is of  $2^{\circ} \times 3^{\circ}$  (latitude× longitude) × 34 levels and the temporal resolution is 6 hours. To distinguish between these two products from CAMS, the analysis product will be referred to as CAMS *hlkx* and the inversion-optimised product as CAMS *v21r1*.

Campaign data was also compared to mixing ratios from six PYVAR-LMDz-SACS (Peng et al. (2022); Lin et al. (2024), abbreviated PLS) ensemble inversions that optimised weekly methane surface fluxes for 2021 at a spatial resolution of  $1.9^{\circ}$ ×

3.75° on 39 vertical levels and 3-hourly time resolution. Inversions employed three different atmospheric observation datasets for flux constraints and two physical parameterisations. Two inversions used GOSAT column estimates to constrain fluxes, either from the National Institute for Environmental Studies (NIES) or University of Leicester (UoL) and the others used in-situ measurements from both the Integrated Carbon Observation System (ICOS) and NOAA tower networks. The two physical parameterisation are known as the "classic" and "advanced" versions of the atmospheric transport model LMDz (noted a and b respectively). The "classic" version uses the vertical diffusion scheme of Louis (1979) and the scheme of Tiedtke (1989) to parametrise deep convection, whilst the "advanced" version combines the vertical diffusion scheme of Mellor and Yamada (1974) and thermal plume modelling by Rio and Hourdin (2008) to simulate the atmospheric mixing in the boundary layer. Deep convection is represented using the scheme from Emanuel (1991) coupled with the parameterisation of cold pools developed by Grandpeix et al. (2010). Bottom-up inventories or process-based land surface models were used to build prior CH<sub>4</sub> fluxes for different categories, and the OH and O(\frac{1}{D}) fields were prescribed from the simulation of a chemistry-climate model LMDz-INCA with a full tropospheric photochemistry scheme. Inclusion of observations and definition of observation errors to constrain fluxes followed the method outlined in (Peng et al., 2022; Lin et al., 2024).

# 2.2.3 Regional atmospheric model (WRF-Chem)

# WRF-Chem configuration

180

185

190

195

200

In addition to global model outputs, the Weather Research and Forecasting coupled with Chemistry (WRF-Chem) model was used to simulate the meteorological conditions and greenhouse gas mixing ratios during the MAGIC2021 campaign on a regional scale. WRF is a widely used mesoscale numerical weather prediction system in both research purposes and operational forecasting. It uses fully compressible and non-hydrostatic Eulerian equations on an Arakawa C-staggered grid to ensure the preservation of mass, momentum, entropy, and scalars (Skamarock et al., 2008). The set-up for this study included two domains, one parent and one nested. The parent domain (d01) encompassed the whole of Fennoscandia as well as Denmark, the westernmost part of Russia and most of the area covered by Baltic countries, at a resolution of 9×9 km. The nested domain (d02) had a higher resolution of 3×3 km and spanned most of the northern part of Finland, Sweden and Norway where MAGIC2021 measurements were taken. Domain boundaries were chosen such as to avoid strong emissions and high topography close to a boundary, which are known to cause transport problems (NCAR, 2024). WRF-Chem generated output fields including meteorological variables and mixing ratios every 20 minutes.

The physical parameterisation included the WSM5 scheme for microphysics (Hong et al., 2004) as well as the RRTMG longwave and shortwave schemes (Iacono et al., 2008) for radiation. The planetary boundary layer was represented using the MYNN Level 2.5 scheme (Nakanishi and Niino, 2009), whilst the revised MM5 surface layer scheme (Jiménez et al., 2012) was used, with the thermal roughness length dependent on vegetation. No urban model was activated. For the land surface, the Noah model was used, with 4 soil layers (Tewari, 2004). Regarding convection, the Kain-Fritsch scheme was used for the parent domain (Kain, 2004), whilst convection was resolved explicitly in the nested domain. Additional convection-related options were activated, including radiation feedback on convection, convection diagnostics, and Grell-Devenyi scheme parameters (Grell and Dévényi, 2002). Vertically, the simulations had 50 levels from ~140m to ~20km with about half of all levels below

2km. The model configuration was evaluated in previous studies to produce minimum transport errors at both continental (Feng et al., 2019) and regional (Díaz-Isaac et al., 2018) scales.

Methane mixing ratios were modelled as passive tracers, which were transported online at each time step concurrently with meteorological variables. Emissions are injected from the surface into the first atmospheric layer to generate the mixing ratio fields of tracers. These tracers undertook a series of transport processes, including advection, diffusion, turbulence, and convective mixing, to simulate the motion of molecules in the atmosphere. Initial conditions were set by ERA5 reanalysis meteorology at  $0.5^{\circ} \times 0.5^{\circ} \times 137$  levels resolution and boundary meteorological conditions were updated every 3 hours using the same product. Data within WRF-Chem domain was then produced by WRF physics and dynamics. Methane boundary conditions were produced by the inversion optimised CAMS mixing ratios product version 21r1 described earlier, at a resolution of  $3^{\circ} \times 2^{\circ} \times 34$  levels every 6 hours. Emissions within simulation domains were divided into multiple tracers depending on source types. These tracers are described in Table 1. mixing ratios within our simulation domain were initially set to a constant value. A period of 15 days was shown to be sufficient for boundary conditions and local emissions to propagate through our domains and reach steady-state. The simulations were thus run from 01/08/2021 to 31/08/2021, to account for spin-up time and the MAGIC2021 campaign period.

**Table 1.** Emission sources used in the WRF-Chem simulations, given with spatial and temporal resolutions as well as emission statistics. Statistics are computed for the larger (d01) WRF-Chem domain over the month of August 2021 or climatological August depending on data availability.

Source	Model	Spatial resolution	Time resolution	Emissions scale (mol·km <sup>-2</sup> ·h <sup>-1</sup> )					
Source	Wiodei	Spatial lesolution	Time resolution	Min	Max	Mean	Median		
Anthropogenic	CAMS	0.1°×0.1°	monthly clim. (2016-18)	0.0	11 000	7.1	0.20		
Fire	CAMS	0.1°×0.1°	daily aug. 2021	0.0	910	0.0	0.0		
Oceanic	Weber et al. (2019)	0.25°×0.25°	monthly clim. (1980-2016)	-0.10	15	0.50	0.0		
Wetland	WetCHARTs 2913	0.5°×0.5°	monthly clim. (2016-18)	0.0	430	12	0.02		
Wetland	WetCHARTs 2914	0.5°×0.5°	monthly clim. (2016-18)	0.0	400	26	0.01		
Wetland	WetCHARTs 2924	0.5°×0.5°	monthly clim. (2016-18)	0.0	300	15	0.01		
Wetland	WetCHARTs 2934	0.5°×0.5°	monthly clim. (2016-18)	0.0	240	11	0.01		
Wetland	WetCHARTs 1913	0.5°×0.5°	monthly clim. (2016-18)	0.0	360	9.6	0.01		
Wetland	WetCHARTs 2923	0.5°×0.5°	monthly clim. (2016-18)	0.0	360	7.9	0.01		
Wetland	WetCHARTs 3913	0.5°×0.5°	monthly clim. (2016-18)	0.0	604	16	0.02		
Wetland	WetCHARTs 3933	0.5°×0.5°	monthly clim. (2016-18)	0.0	350	6.8	0.01		
Wetland	JSB-HIM(CRU)	0.1°×0.1°	daily aug. 2021	0.0	190	10	0.32		
Wetland	JSB-HIM(CRU4)	0.1°×0.1°	daily aug. 2021	0.0	140	6.4	0.15		
Wetland	JSB-HIM(ERA5)	0.1°×0.1°	daily aug. 2021	0.0	170	4.8	0.02		
Lakes	Johnson et al. (2022)	0.25°×0.25°	daily clim. 2003-2015	0.0	$2.0 \times 10^{-10}$	$5.6 \times 10^{-12}$	$2.2 \times 10^{-13}$		

# Emission tracers

220

205

210

215

Input emissions (Table 1) were chosen according to data availability for August 2021, then prioritising higher spatial resolution in order to reduce regridding issues. If no product were found for that time period, the highest time resolution product was chosen and climatological averages were used.

Oceanic methane emissions were taken from Weber et al. (2019), a monthly climatology with a spatial resolution of  $0.25^{\circ} \times 0.25^{\circ}$ . Methane lake emissions from Johnson et al. (2022) were also used. The dataset includes corrections for daily and seasonal observational bias, observed ice-free/emission seasonality, and realistic lake area and distribution. Anthropogenic and fire emissions of methane were provided by CAMS, which publishes emissions driving their global atmospheric greenhouse gas mixing ratios products (Agustí-Panareda et al., 2023). They are respectively from EDGARv4.2FT2010 (Olivier and Janssens-Maenhout, 2012) and GFAS Version 1.2 (Kaiser et al., 2012). Anthropogenic and fire emissions both share the same  $0.1^{\circ} \times 0.1^{\circ}$  spatial resolution but anthropogenic emissions were monthly averaged emissions over 2016-2017-2018 (latest years available) whereas fire emissions were daily emissions from August 2021. Wetland emissions came from two sources: the latest product from the WetCHARTs model (Bloom et al., 2017), with simulations up to 2019, and several versions of JSBACH-HIMMELI (JSB-HIM) simulations originally designed for the European project VERIFY, described in Aalto (2019), that were recently extended to later years. WetCHARTs has a spatial resolution of  $0.5^{\circ} \times 0.5^{\circ}$  and a monthly time resolution, spanning until 2019. A monthly climatological average was therefore used, taking the same years as for CAMS anthropogenic emissions. 18 different flux versions are publicly available from WetCHARTs, depending on physical parameters detailed in the documentation (Bloom et al., 2017). A subset of 8 WetCHARTs versions were selected, to maximise representativeness of the dataset whilst staying cost-effective in our computations. JSB-HIM emissions were provided by the Finnish Meteorological Institute (FMI) at daily resolution for August 2021 and a spatial resolution of  $0.1^{\circ} \times 0.1^{\circ}$ . 3 versions of total wetland flux from JSB-HIM, each differing in their driving meteorology were included in this study.

225

230

235

240

245

250

Inventory emissions all have different spatial resolution, so they have to be regridded to our WRF-Chem domains resolution. This was done by interpolating emissions from our data products to the WRF-Chem grid (Virtanen, 2010). 11 emission tracers and one boundary condition tracer were tracked in the simulation of total regional CH<sub>4</sub> mixing ratios. Boundary conditions were provided by the inversion-optimised CAMS v21r1 product described in Section 2.2.2 and interpolated onto WRF-Chem vertical levels using Lauvaux (2022). Additionally, artificial boundary conditions were also implemented for other tracers in order to prevent near-zero computation error propagation throughout the whole simulation. This was done by adding a constant offset of 300ppb through the emission tracers domain boundaries on an hourly basis. WRF-Chem supports several independent passive tracers. This allows us to construct different versions of atmospheric methane mixing ratios from a single simulation. A common core of methane mixing ratios was built using the boundary condition tracer added to the sum of anthropogenic, fire, oceanic and lake emissions tracers. To this common core, wetland contributions can be separately added to obtain different atmospheric methane mixing ratios. These wetland emissions include 8 separate products from the WetCHARTs inventory, and 3 products from JSB-HIM simulations as described above (Bloom et al., 2017; Aalto, 2019). Simulations were run in both d01 and d02 domains, resulting in a total of 22 atmospheric CH<sub>4</sub> mixing ratios product.

**Table 2.** Model specifications for simulations used in this study.  $\eta$  vertical coordinates are a hybrid sigma-pressure coordinate. Meteorologicalonstraints can be from in-situ measurements such as weather balloons or measurement towers. For CH<sub>4</sub> we use surface to specify that constraints come from surface mixing ratio measurements.

Model	Туре	Resolution	Transport	Constraints
ERA5	global NWP	$0.25^{\circ} \times 0.25^{\circ} \times 137 \eta \times 1h$	IFS	in-situ + satellite (Hersbach et al., 2020)
CAMS hlkx	global CTM analysis	$0.25^{\circ} \times 0.25^{\circ} \times 137 \eta \times 6h$	IFS	in-situ + satellite (Peuch et al., 2022)
CAMS v21r1	global CTM inversion opt.	$2^{\circ} \times 3^{\circ} \times 34 \eta \times 6h$	TM5	surface (Segers, 2023)
PLS	global CTM inversion opt.	$1.9^{\circ} \times 3.75^{\circ} \times 39 \eta \times 3h$	LMDz	surface or satellite (Lin et al., 2023)
WRF-Chem	regional NWP + CTM	$d01(d02)$ : 9(3) km×9(3) km×50 $\eta$ ×1h	WRF	CAMS v21r1 boundary conditions

# 2.3 Comparison method

255

260

265

## 2.3.1 4 dimensional barycentric interpolation using Delaunay triangulation

In our comparisons, modelled data were interpolated on measurement locations using the python function <code>scipy.interpol-ate.griddata</code> from the scientific python library <code>scipy</code>. The function <code>griddata</code> uses <code>scipy.interpolate.Linear-NDInterpolator</code> when performing linear interpolation in multiple dimensions as in our case, a function that was written in cython by Virtanen (2010). Interpolation is necessary because gridded modelled data do not have the same temporal or spatial resolution as measurements taken by balloons or aircraft. Additionally, using Delaunay triangulation as in <code>griddata</code> allows interpolation from an irregular grid such as the pressure grid used in studied models. The interpolation was performed in 4 dimensions (time + 3 space dimensions). <code>griddata</code> first computes a Delaunay triangulation around the measurement coordinates to pick out interpolating points from the model grid. In 4 dimensions, each simplex around an observation point contains 5 vertices corresponding to 5 model coordinates in 4D. Barycentric linear interpolation is then performed using each simplex's 5 vertices to compute a model value at a particular measurement location. This method enables a fast, easy to implement and accurate comparison between modelled and measured data, by allowing comparison along each instrument's individual trajectory.

#### 2.3.2 Layer analysis and statistical metrics

Our analysis systematically divided comparisons in 3 layers: the boundary layer (BL), free troposphere (FT) and lower stratosphere (LS). MAGIC2021 data and interpolated model data was categorised as within the BL if the measurement height was below the BL height as computed by ERA5, interpolated at the measurement location. The FT layer extended from the BL height up to the tropopause, which was only reached by weather balloons. Tropopause height was derived from observational data using the cold-point tropopause (CPT) method (Eugenio and Macalalad, 2021).

Four statistical metrics were computed to assess model performance against observations in each of the three previously defined layers and to compare the performance of models. In the following, we note the model bias  $\overline{\Delta}$  from Willmott (1982), which is the mean difference between interpolated model quantities and measured physical quantities over a sample of mea-

surements, standard deviation  $\sigma$ , Pearson correlation  $\rho$ , and root-mean-square error RMSE. Circular statistics from Mardia (1972); Jammalamadaka and Sengupta (2001) were applied to compare wind directions by computing circular  $\overline{\Delta}$ ,  $\sigma$ ,  $\rho$  and RMSE associated with model and observed directions.

These metrics were used to draw Taylor diagrams (Taylor, 2001) which allow to assess a set of models against observations. These diagrams cleverly combine  $\rho$ ,  $\sigma$  and centred RMSE (CRMSE) in a polar coordinate plot using the law of cosines. The radial coordinate of a data point usually represents the standard deviation ( $r = \sigma$ ) whilst angular position gives its correlation with observations ( $\alpha = \arccos(\rho)$ ). A reference point is set at ( $\sigma_{\rm obs}$ ,  $\rho_{\rm obs}$ ) where  $\sigma_{\rm obs}$  is the standard deviation of the observations and  $\rho_{\rm obs} = 1$ . Here we normalise  $\sigma$  to be able to compare quantities from different layers of the atmosphere onto the same plot:  $\sigma_{\rm N} = \sigma/\sigma_{\rm obs}$ . The coordinates of the reference point become (1,1). The better the model, the closer to this reference point it will be. CRMSE can also be represented on the diagram, as the radial distance from the reference point. Taylor (2001) shows:

$$\text{CRMSE} = \sqrt{\frac{1}{N} \sum_{i}^{N} \left[ (x_i^{\text{obs}} - \overline{x^{\text{obs}}}) - (x_i^{\text{mod}} - \overline{x^{\text{mod}}}) \right]^2} = \sqrt{\sigma_{\text{obs}}^2 + \sigma_{\text{mod}}^2 - \rho \sigma_{\text{obs}} \sigma_{\text{mod}}}$$

This metric is a measure of model spread around observational values after removing any bias. It is therefore useful to quantify model noise but it lacks an assessment of distance between model estimates and observations. To remedy this, we chose to pair each Taylor diagram with a plot of RMSE against  $\overline{\Delta}$  as in Kärnä and Baptista (2016).

# 3 Weather data comparison: Results & Discussion

#### 3.1 Horizontal wind

280

285

290

295

Relatively high noise was observed in vertical wind measurements from aircrafts and radiosoundings, particularly when compared to the low magnitudes of the measured values. Moreover, several issues in the radiosounding data, such as unphysical steps in the recorded values, led us to exclude vertical wind data from our comparisons.

Figure 2 shows that both ERA5 and WRF manage to generally capture the observed dominant wind directions. For example, models and observations agree on a contribution superior to 20% from notherly winds in the free troposphere. In the BL, observed winds are divided in 5 northerly and southerly main components, which all contribute less than 20% of the sampled winds. ERA5 reproduces this distribution well, with multiple wind directions involved in low proportions while WRF over-represents contributions from the main wind components (more than 30% of northerly winds in the BL). This pattern is also observed in the LS and to a lesser extent in the FT.

Overall, ERA5 performs better in reproducing observed wind speed distributions, particularly in the mid-troposphere, and provides a more balanced representation of secondary wind directions at higher altitudes. WRF, on the other hand, tends to overrepresent dominant wind components while underrepresenting secondary contributions, with consistent patterns across its two domains. We now look at the statistical performance of these models in terms of wind speed and direction separately.

ERA5 generally outperformed WRF in wind speed metrics across the three atmospheric layers, as shown in Figure 3. It ranked first in normalized standard deviation ( $\sigma_N$ ) and RMSE for all layers, as well as in correlation ( $\rho$ ) for the BL and FT.

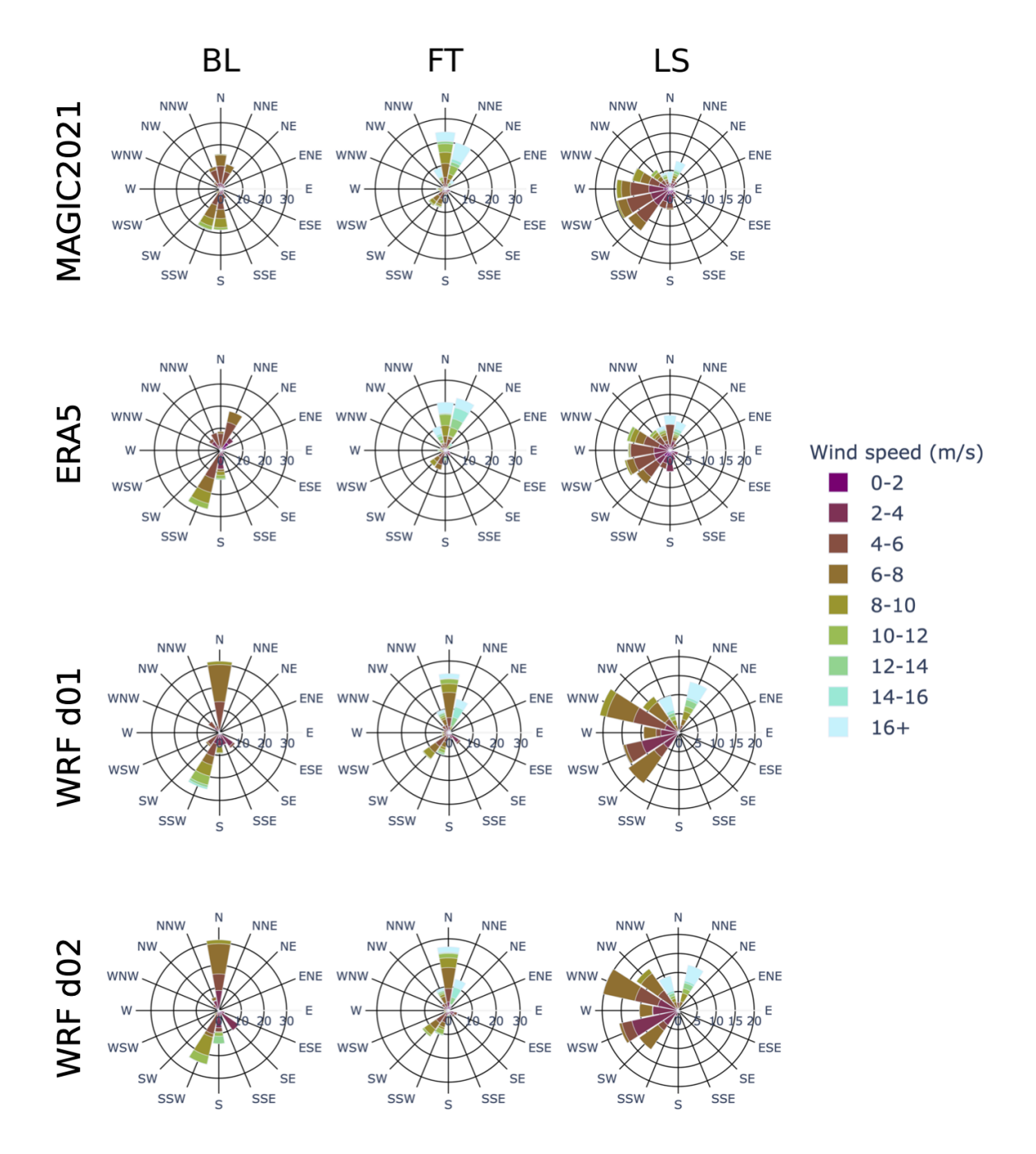


**Figure 2.** Wind rose plots for MAGIC2021 observations as well as ERA5 and WRF simulations. The radial axis gives the proportion (in %) of wind coming from a given direction given by the angular axis. Coloured bins represent the share of speed ranges shown in the legend associated with each direction. Rows correspond to data products MAGIC2021 observations, ERA5, WRF d01 and WRF d02. Columns correspond to atmospheric layers: Boundary Layer (BL), Free Troposphere (FT) and Lower Stratosphere (LS), described in Section 2.3.2.

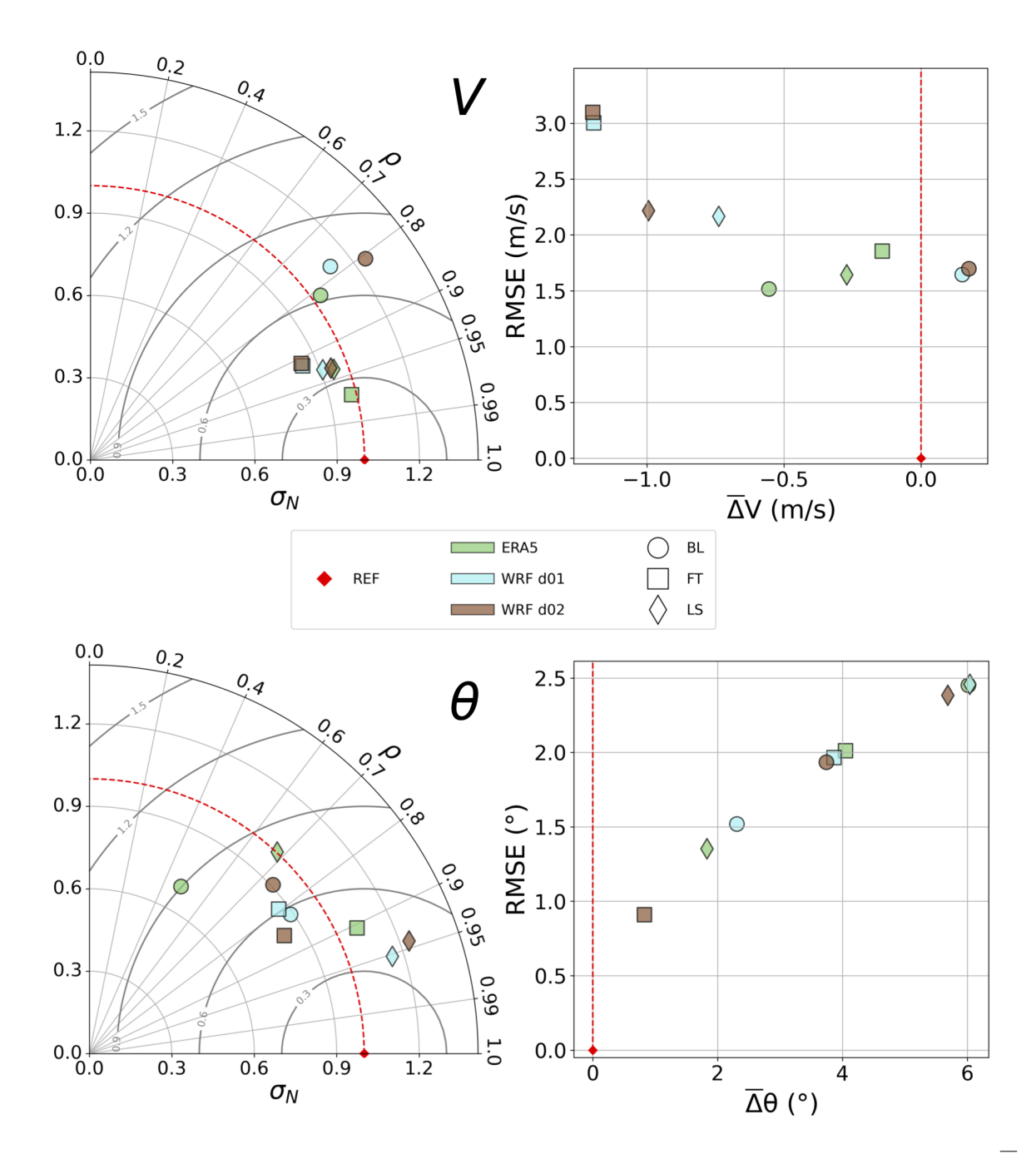


Figure 3. Comparison between simulated and observed wind speed V (top) and direction  $\theta$  (bottom) with Taylor (left) and bias  $(\overline{\Delta})$  versus RMSE (right) diagrams. The radial axis of Taylor diagrams represents the normalised standard deviation of modelled wind speed/direction. The angular axis represents correlation between modelled and observed wind speed/direction. Centred RMSE is represented by the radial distance from the reference point. RMSE and bias are computed subtracting observed quantities to simulated quantities.

Specifically, ERA5 achieved a top rank in 75% of wind speed metrics (9 out of 12, Table 3), compared to WRF d01 (16.7%) and WRF d02 (8.3%). For example, in the BL, ERA5 ranked first in  $\sigma_N$ ,  $\rho$ , and RMSE, though it ranked third in bias  $(\overline{\Delta})$ , where WRF d01 performed best. Similarly, in the FT, ERA5 maintained its top position across all wind speed metrics except for  $\overline{\Delta}$ , where WRF d01 ranked first. In the LS, ERA5 continued to rank first in  $\sigma_N$ , RMSE, and  $\overline{\Delta}$  but fell short in  $\rho$ , where WRF d01 and d02 performed better. These results highlight ERA5's consistent strength in reproducing observed wind speeds in all metrics.

For wind direction, as illustrated in Figure 3, ERA5 and WRF showed more mixed performance. While ERA5 ranked first for some metrics in the FT and LS, WRF d01 performed better especially in the BL and LS, achieving the highest correlation ( $\rho$ ) and lowest RMSE in both layers. In the BL, WRF d01 also demonstrated strong performance in other metrics, ranking first in  $\rho$  and  $\overline{\Delta}$ . Notably, WRF d01 outperformed the finer domain (d02) in 75% of wind direction rankings (9 out of 12, Table 3), indicating that the coarser domain was often better suited for capturing wind direction variability and error. ERA5, on the other hand, exhibited varying performance across layers, with error metrics  $\overline{\Delta}$  and RMSE rank changing with altitude (e.g. third in  $\overline{\Delta}$  & RMSE in the BL and FT but first in the LS).

Overall, ERA5 exhibited superior performance in wind speed metrics across most layers, while WRF d01 showed stronger results for wind direction, particularly in the BL and LS. The relative performance of each model is summarised in Table 3. The table ranks each model against the other 2 for each physical quantity, statistical metric and atmospheric layer studied. A colour code is also given as a visual aid (green for position 1, yellow for position 2 and red for position 3). Our model assessment can then be quantified by computing the average rank of each model over all atmospheric layers and statistical metrics. ERA5 had an average rank of 1.17 in terms of wind speed, in contrast to WRF d01 (2.08) and WRF d02 (2.75). For wind direction however, both WRF d01 and d02 outperformed ERA5, with the same average rank of 1.92, compared to 2.17 for ERA5.

# 3.2 Temperature

305

310

315

Figure 4 shows temperature profiles on the upper part of the figure and temperature bias ( $\overline{\Delta}$ ) profiles on the lower part. Here the MAGIC2021 dataset is compared to ERA5, WRF d01 and WRF d02. Bias is computed such that a positive  $\overline{\Delta}T$  means that modelled temperature was superior to observations on average over all MAGIC2021 measurements in the particular bin considered. The lower-most part of the left profiles, which compare temperatures above P = 800hPa, shows a negative bias of ~3 °C for all three models. Further investigation of model performance against each instrument separately shows that this bias was only present against AirCore data, while no significant bias was observed with other instruments, which suggests that there could have been an issue with AirCore data near the surface. In the middle section (800>P>300hPa), models and observations follow consistently the negative vertical gradient, with ERA5 better capturing profile features, which is allowed by its better vertical resolution. Finally, in the lowest pressure levels, a good agreement between ERA5, WRF and MAGIC2021 T was found, but with more variation around  $\overline{\Delta}T = 0$  for WRF. WRF values cannot be compared to weather balloon data in the LS above P≈50 hPa as this was set as the upper limit of the model domain. Overall, modelled temperatures reproduce well the temperatures measured during the campaign, with a mean bias consistently inferior to 2 °C across all layers.

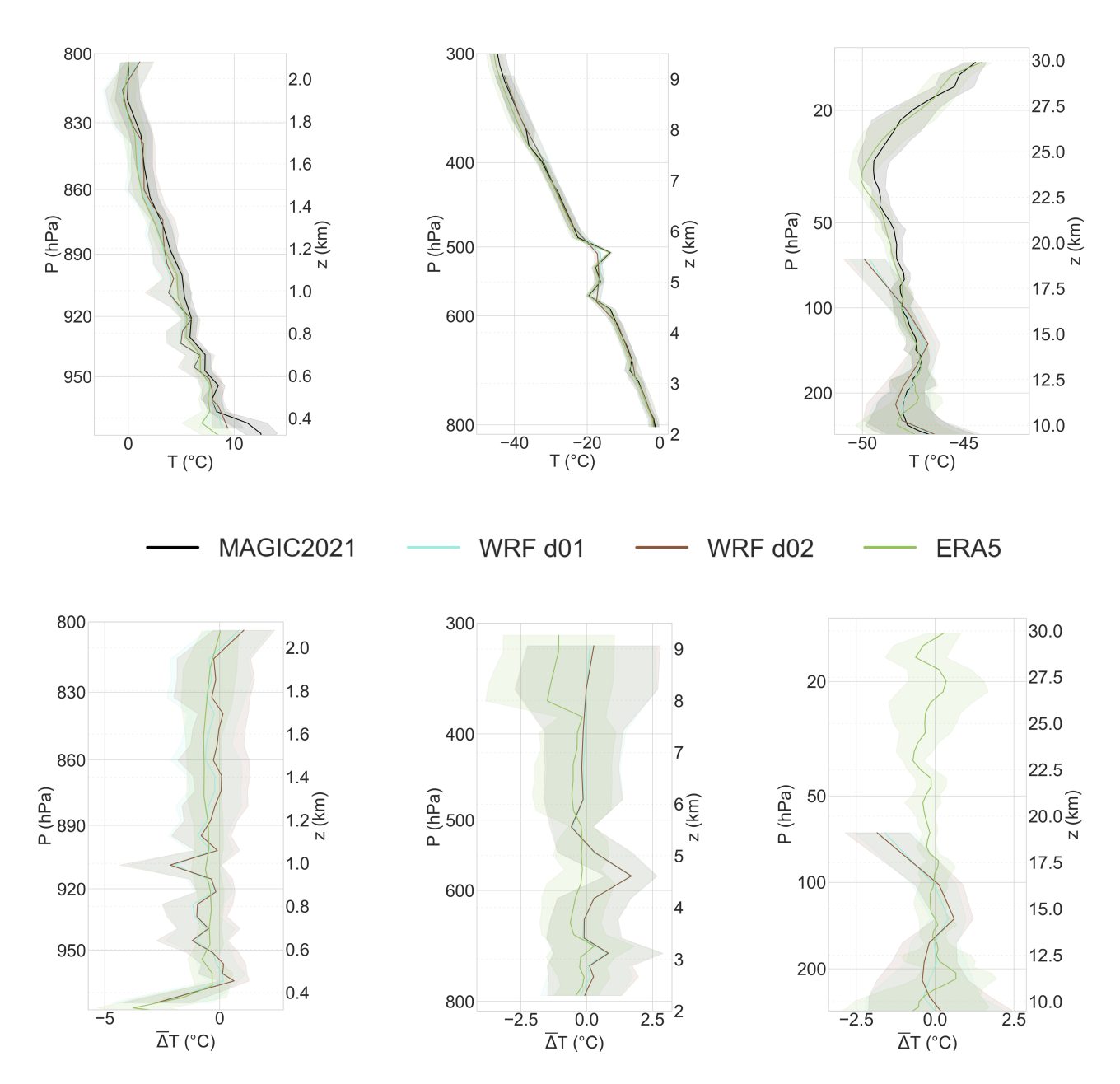


Figure 4. Vertical temperature intercomparison between MAGIC2021 data and weather models. Observational data includes MAGIC2021 data from weather balloons, ATR42 and Cessna aircraft and was binned to fit model grids. Profiles are divided in three blocks (P>800hPa, 300</br> 300<br/> 400<br/> 400<br/

Figure 6 shows the statistical intercomparison with all models, metrics and atmospheric layers for both temperature and humidity (RH), the top panel focusing on temperature. It can be seen that all models performed very well in every layer, being all close to  $\sigma_N=1$  and correlating very well with observations ( $\rho \geq 0.8$ ). In terms of RMSE and  $\overline{\Delta}$ , models also perform well, with RMSE < 2°C and  $\overline{\Delta}$  < 1 °C in all layers. Models generally reproduce temperature best in the FT, followed by the LS, and then the BL across most statistical categories.

Table 3 shows that ERA5 performed better than both WRF domains in most statistical categories and layers in terms of temperature as well, with an average rank of 1.17 for ERA5 versus an average rank > 2 for WRF. Overall, WRF d01 and d02 showed closely similar performance in all layers, with WRF d01 slightly but consistently outperforming d02 in most statistical metrics and layers (average rank of 2.08 for WRF d01 and 2.75 for d02).

# 3.3 Humidity

340

345

350

355

360

365

As for temperature, relative humidity profiles for ERA5, WRF d01 and WRF d02 are shown on Figure 5. The top panel shows the mean RH profile observed during MAGIC2021 and the corresponding mean interpolated profiles for each model. The bottom panel shows the corresponding bias profiles. The left handside profiles show that humidity increased with height on average from the surface up to about z = 1.5 km, which was well captured by all models. The bias profiles also suggest RH<sub>ERA5</sub> > RH<sub>WRFd01</sub> > RH<sub>WRFd02</sub> throughout the highest pressure levels. In the middle block, the models also captured the decrease in RH with height well; however, the previously observed tendency of higher RH values in ERA5 compared to WRF d01 and WRF d02, is no longer there. At lower pressure levels, RH strongly decreased with height and reaches  $\sim$ 0% just below z = 15 km which was captured by all models but with an underestimation of the observed RH values between 10 and 12 km.

The bottom panel of Figure 6 shows the full statistical intercomparison with 4 metrics and 3 layers (BL, FT and LS) for relative humidity. Models correlated best with MAGIC2021 measurements in the LS and FT, and less in the BL. Variability was also generally better represented in the FT and LS than in the BL, with  $\sigma_N$  being closer to 1. Model performance was good overall, but showing worst numbers than for temperature.  $\sigma_N$  values ranged from 0.75 to 1.4 and  $\rho$  went from just under 0.65 in the BL to  $\sim$ 0.9 in the FT. ERA5 performed once again better both in terms of correlation and  $\sigma_N$  than WRF in all layers. In terms of RMSE, RH was least well represented in the FT, where a RMSE > 12% was observed for all models. The BL was where bias was highest, at around 2% on average, depending on the model. For WRF, the bias observed in the BL was opposite to the bias in the FT. All models showed their best performance in terms of RMSE and bias in the LS, due to the low values of RH at this altitude. ERA5 showed consistently better performance in terms of RMSE and bias whilst WRF d01 and d02 showed better  $\sigma_N$  performance in the FT and LS respectively.

These results are summarised in Table 3 where ERA5 gets the first position in all layers and metrics, except for  $\sigma_N$  in the LS, where WRF d01 and d02 did not simulate RH up to the same height as ERA5, which could explain the better performance of WRF in that layer. The overall performance of WRF d01 and d02 was similar, but WRF d01 did outperform d02 in terms of average rank (2.17 for d01 versus 2.67 for d02).

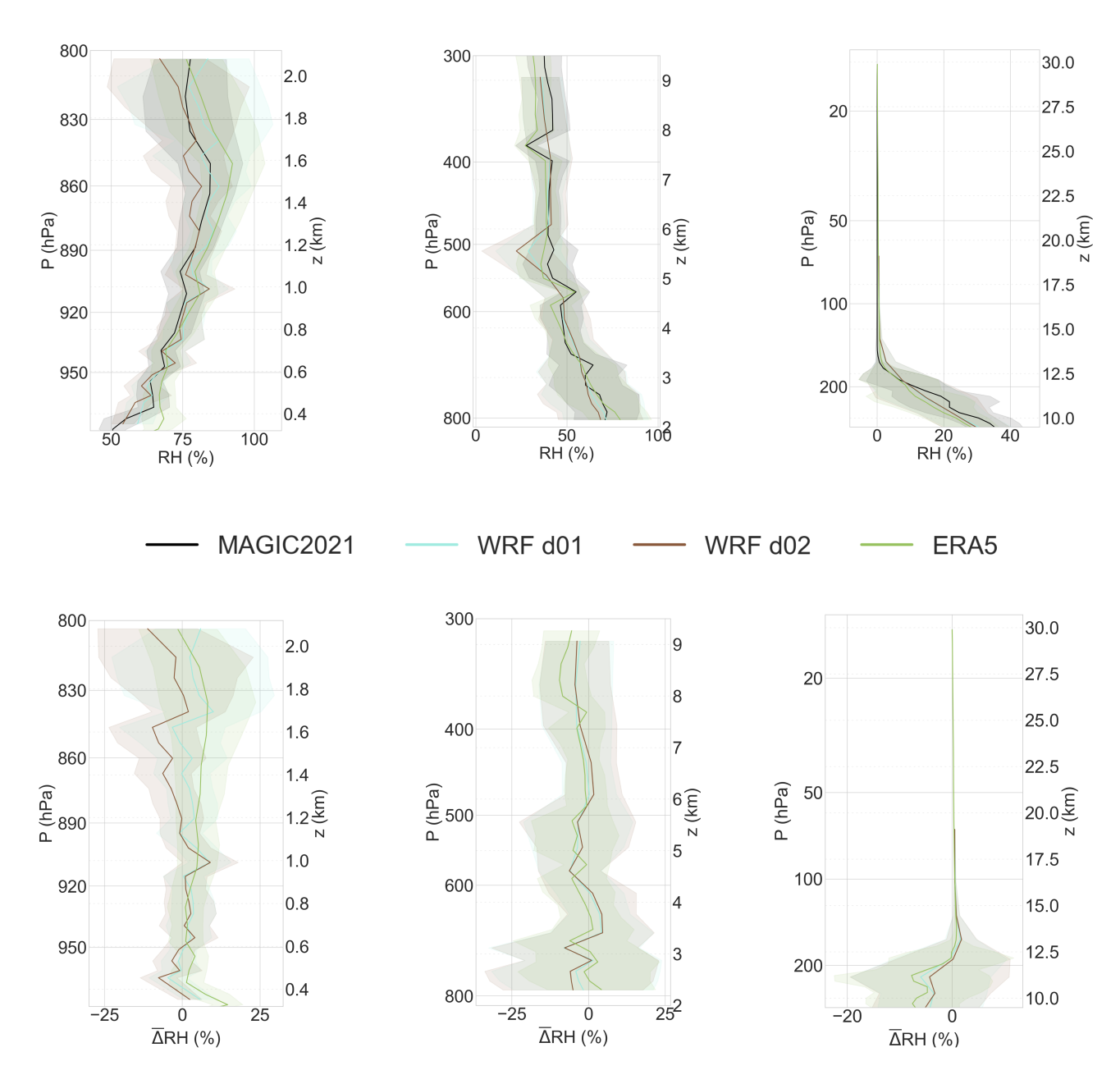


**Figure 5.** Vertical relative humidity intercomparison between MAGIC2021 data and weather models. Observational data includes MAGIC2021 data from weather balloons, ATR42 and Cessna aircraft and was binned to fit model grids. Profiles are divided in three blocks (P>800hPa, 300<P<800hPa and P<300hPa) which allow to illustrate results from our analysis layers (BL, FT, LS). Shaded areas represent the 1- $\sigma$  deviation from the mean RH or RH bias profiles, computed from binned data. **Top:** Mean RH profiles computed accross all flights from MAGIC2021 platforms (black) plotted with mean interpolated RH profiles from models corresponding to platform trajectories. **Bottom:** Bias profiles in the same pressure ranges. Bias is computed as the mean difference between interpolated model quantities and measured physical quantities over each bin.

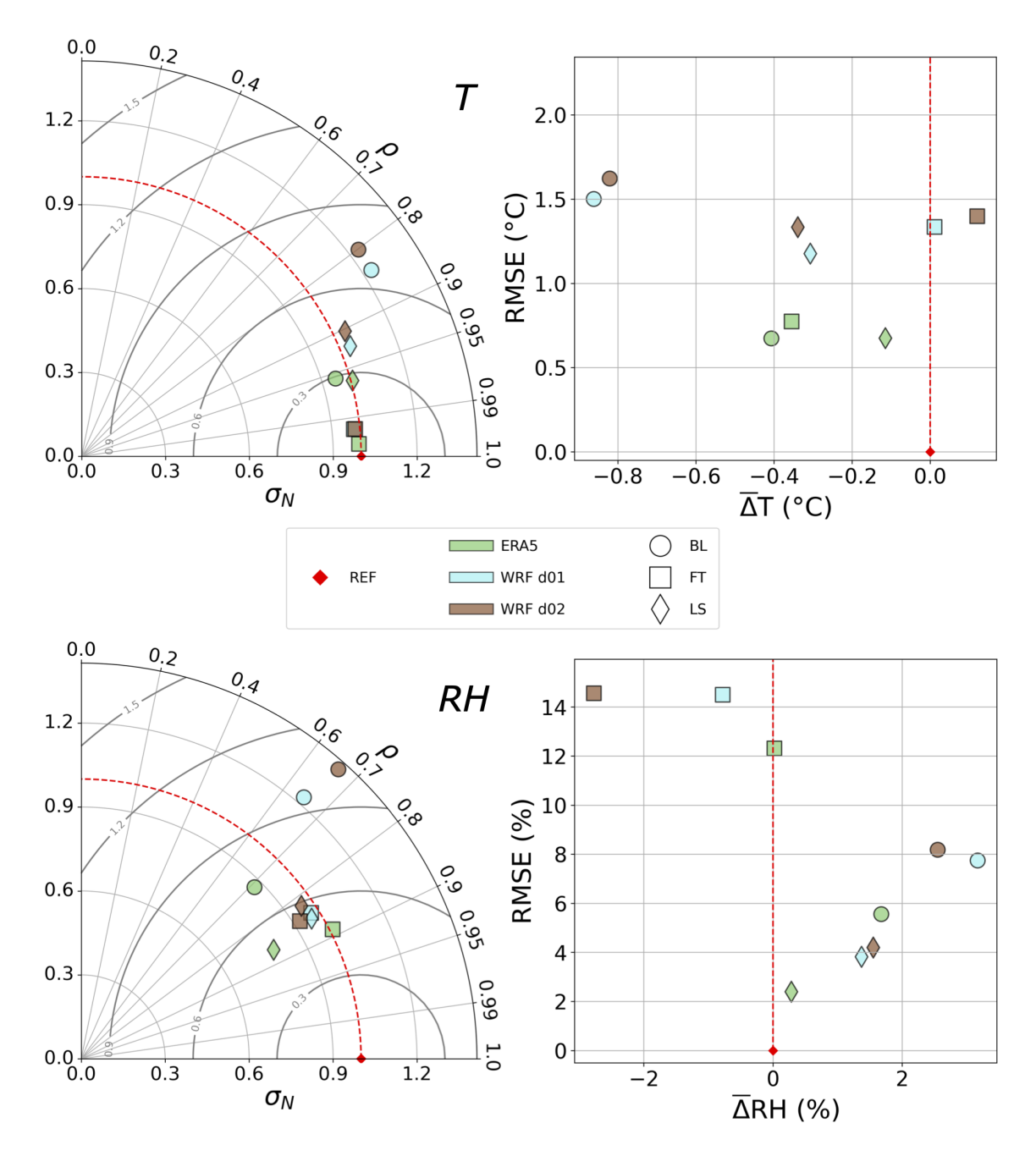


Figure 6. Comparison between simulated and observed temperature (top) and relative humidity (bottom) with Taylor (left) and bias  $(\overline{\Delta})$  versus RMSE (right) diagrams. The radial axis of Taylor diagrams represents the normalised standard deviation of modelled T/RH. The angular axis represents correlation between modelled and observed T/RH. Centred RMSE is represented by the radial distance from the reference point. RMSE and bias are computed subtracting observed quantities to simulated quantities.

**Table 3.** Simulation rank depending on the meteorological quantity assessed for the three atmospheric layers and the four statistical metrics considered in the study. Spd refers to wind speed, Dir to wind direction, T to temperature and RH to relative humidity comparisons.

			Rank	$\sigma_N$			Ranl	ς ρ		F	Rank R	MSI	3		Rank	$\overline{\Delta}$	
		Spd	Dir	T	RH	Spd	Dir	T	RH	Spd	Dir	T	RH	Spd	Dir	T	RH
ERA5	BL	1	3	1	1	1	3	1	1	3	3	1	1	1	3	1	1
	FT	1	1	1	1	1	1	1	1	1	3	3	1	1	3	1	1
	UTLS	1	1	1	3	1	3	1	1	1	1	1	1	1	1	1	1
WRF d01	BL	2	2	2	2	3	1	2	3	1	1	2	3	2	1	3	2
	FT	2	2	3	2	2	3	2	3	2	2	1	2	2	2	2	2
	UTLS	3	2	2	1	3	1	2	2	2	3	2	2	2	3	2	2
WRF d02	BL	3	1	3	3	2	2	3	2	2	2	3	2	3	2	2	3
	FT	3	3	2	3	3	2	3	2	3	1	2	3	3	1	3	3
	UTLS	2	3	3	2	2	2	3	3	3	2	3	3	3	2	3	3

## 3.4 Conclusions on weather data comparison

370

375

380

385

The good performance of both ERA5 and WRF in terms of horizontal wind speed and direction was not surprising as they are widely used and well validated models. ERA5 speed scores were better than both WRF d01 and d02, and direction scores were about equivalent even though both WRF domain slightly outperformed ERA5. Over all physical quantities, atmospheric layers and statistical metrics, ERA5 obtained an average rank of 1.42, WRF d01 a rank of 2.06 and WRF d02 a rank of 2.52. The fact that ERA5 is a reanalysis product could explain its better performance, as it benefits from data assimilation unlike WRF. WRF could be expected to perform better than ERA5 in the boundary layer, given its fine resolution and use of an advanced PBL scheme to model turbulence. In particular,  $\overline{\Delta}$  should get better with higher resolution, however noise related metrics could be expected to get worse as higher resolution implies more potential noise. We indeed found lower  $\overline{\Delta}$  in both wind speed and direction for WRF over ERA5 in the BL. However, performance did not improve significantly between d01 and d02, with d01 even outperforming d02 in bias for wind direction in the BL. Metrics other than  $\overline{\Delta}$  are all influenced by noise even though RMSE and  $\sigma_N$  do not depend solely on it. Thus we use CRMSE, represented by radial distance from the reference point in Taylor diagrams, to assess model noise performance. We find that WRF d01 and d02 have slightly higher CRMSE than ERA5 in the BL & FT for wind speed but not for direction which only partially confirms our hypothesis. Mass et al. (2002); Gómez-Navarro et al. (2015) explained in more detail how higer resolution in simulations can lead to worse performance in objective statistical assessments. They demonstrated that, whilst simulations with finer resolution could enhance the representation of physical processes compared to coarser simulations, they are more significantly influenced by timing and spatial inaccuracies. This explains the better results obtained with ERA5, compared to WRF d01 and WRF d02, also highlighting the challenges involved in validating high-resolution models. It also underscores that employing a range of statistical measures enables more robust evaluations of model performance. WRF outputs can be improved by nudging, which involves adjusting model estimates using observations or reanalysis products, to help regional simulations fit observations better (Bullock et al., 2014), but nudging was not utilised in the WRF runs analysed here, to specifically compare WRF physics to ERA5. Data assimilation could be implemented in our simulations using WRFDA, the data assimilation system included in WRF (Pattanayak and Mohanty, 2018) in order to directly compare model physics, as well as quantifying the impact of data assimilation on simulations in that region.

Assessment of temperature was also characterised by an overall very good performance from all simulations ( $\overline{\Delta}$  < 1K in all layers). Temperatures from weather balloons appear to be slightly biased (by about 2 K) in the BL. This could be due to a lack of corrections of temperatures measured in the boundary layer by the M20. Further checks did not find any correlation between wind speeds and  $\overline{\Delta}$ T as measured by the instrument, so no physical disturbance appeared to have been interferring with measurements. This was unexpected as calibration was performed prior to balloon release on the ground, in that surface layer. It is worth noting that consistent  $\overline{\Delta}$ >0 was only found in some flights (002, 003, 004 on 21/08 and 22/08) that had  $\overline{\Delta}$  > 1K in the BL, the other half of the flights not showing this characteristic. Investigating those particular flights in more detail appears necessary to understand the origin of our findings.

Overall, WRF simulations were close to both ERA5 and MAGIC2021 data in terms of performance, which gives confidence in the ability of the model to simulate the atmosphere in our region of interest.

# 4 Assessment of CH<sub>4</sub> simulations

410

# 405 4.1 Comparison between modelled and observed CH<sub>4</sub> profiles

CH<sub>4</sub> mixing ratio profiles and CH<sub>4</sub> bias profiles ( $\overline{\Delta}$ CH<sub>4</sub>) computed for several models versus MAGIC2021 data are shown on Figure 7. The left profiles show comparisons for P>800 hPa, the middle profiles 800>P>300 hPa and the right profiles for P<300 hPa. Only PLS Surf b results are shown from the 6 different model products, as it performed best overall (details shown in Figure 8, Table 4 and Figure A4). In the P>800 hPa profiles, CH<sub>4</sub> mixing ratios from global models were close to or smaller than CH<sub>4</sub> from MAGIC2021 measurements, while regional models simulated higher CH<sub>4</sub> content than in-situ measurements. This was observed with all three platforms (see Figure A3 for details), with specifically PLS Surf b and CAMS v21r1 showing the best fit to the observed CH<sub>4</sub> mixing ratios while CAMS hlkx CH<sub>4</sub> mixing ratios were negatively biased. Regional simulations from WRF-Chem, mainly influenced by surface emissions in the BL, produced mixing ratios higher than MAGIC2021 measurements (of ~20-100 ppb in d01 and ~20-50 ppb in d02).

In the 800>P>300 hPa profiles, CAMS *hlkx* mixing ratios were consistently below MAGIC2021 measurements, by about 25-50 ppb. PLS Surf b and CAMS *v21r1* simulations performed well again with  $\overline{\Delta}$ CH<sub>4</sub> close to 0 throughout all levels. Regional model biases decreased significantly with altitude (800-300 hPa), reducing the gap between d01 and d02 showing similar bias as CAMS *v21r1* and PLS Surf b.

In the LS, CAMS *hlkx* transitioned from a negative bias in the FT to a strong positive bias exceeding 200 ppb at P∼50 hPa.

PLS Surf b, CAMS *v21r1*, and WRF-Chem displayed more complex bias profiles in this region. They were characterised by a first peak in bias (50-100 ppb) near 250 hPa, followed by a decrease to -50-0 ppb between 175 and 100 hPa, and then a second increase to 100-200 ppb at pressures below 100 hPa. In the FT and LS, WRF-Chem mixing ratios closely followed CAMS

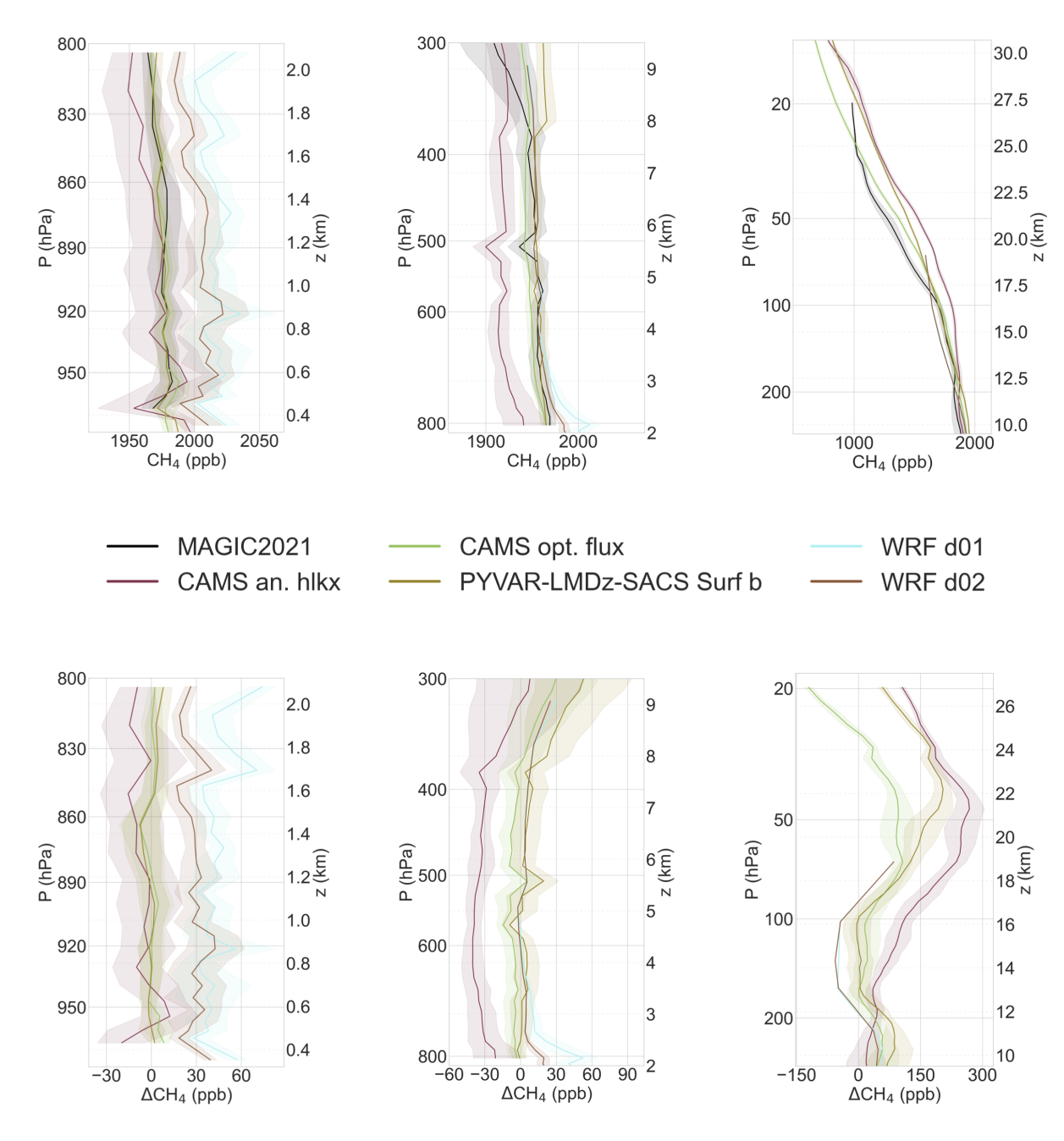


**Figure 7.** Vertical methane intercomparison between MAGIC2021 data and chemistry-transport models. Observational data include MAGIC2021 samples from AirCores, ATR42 and Cessna aircraft and were binned to fit model grids. Profiles are divided in three blocks (P>800hPa, 300<P<800hPa and P<300hPa) which allow to illustrate results from our analysis layers (BL, FT, LS). Shaded areas represent the 1-σ deviation from the mean CH<sub>4</sub> or CH<sub>4</sub> bias profiles, computed from binned data. **Top:** Mean CH<sub>4</sub> profiles computed accross all flights from MAGIC2021 platforms (black) plotted with mean interpolated CH<sub>4</sub> profiles from models corresponding to platform trajectories. **Bottom:** Bias profiles in the same pressure ranges. Bias is computed as the mean difference between interpolated model quantities and measured physical quantities over each bin.

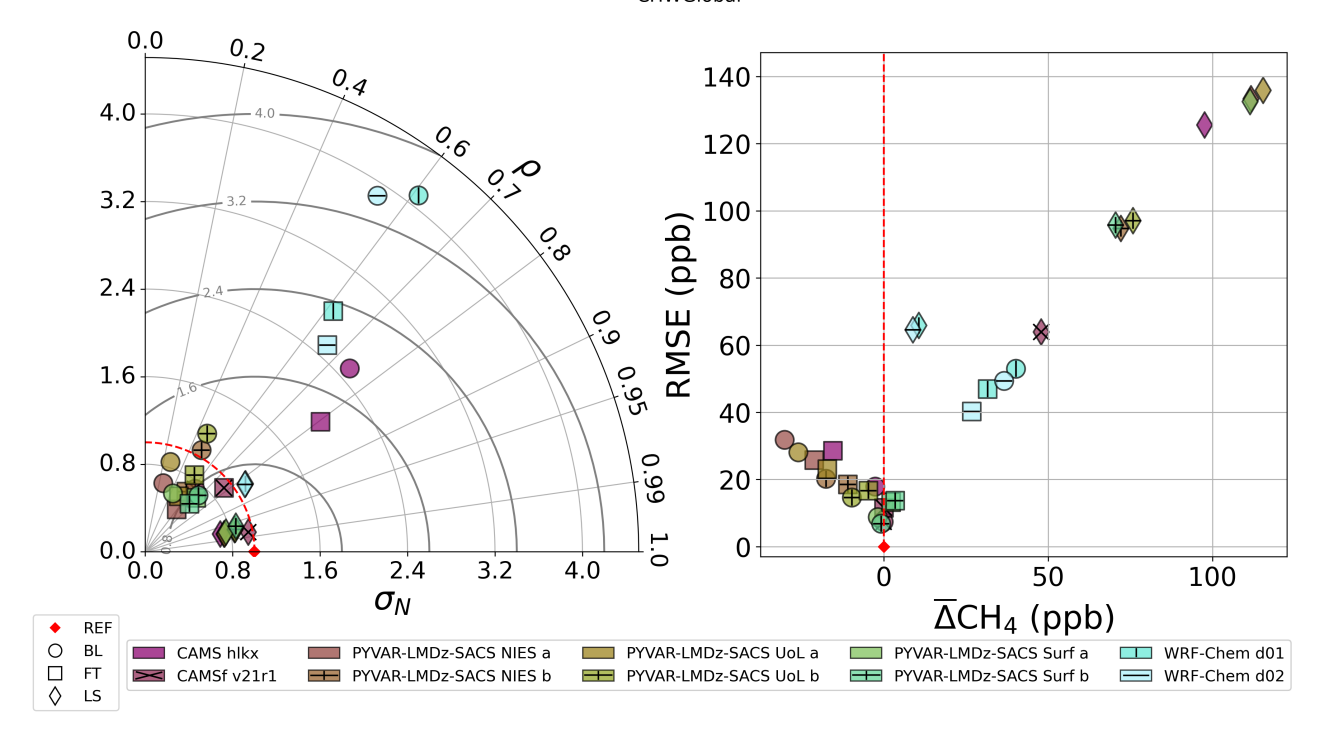


Figure 8. Left: Taylor diagram for CH<sub>4</sub> comparisons between MAGIC2021 observations and ERA5 model. The radial axis represents the normalised standard deviation of the modelled CH<sub>4</sub>. The angular axis represents the correlation between modelled and observed CH<sub>4</sub>. The centred RMSE is represented by the radial distance from the reference point. Right: RMSE against bias ( $\overline{\Delta}$ CH<sub>4</sub>) computed from MAGIC2021 observations and modelled CH<sub>4</sub>. RMSE and bias are computed subtracting observed quantities to simulated quantities.

*v21r1* (product that was used as boundary conditions). A deviation from this behaviour was observed in the LS above the first peak in bias at approximately 300 hPa, likely due to transport differences between WRF-Chem and TM5 (the transport model used in CAMS *v21r1*).

425

430

Figure 8 shows results from the comparison between MAGIC2021 CH<sub>4</sub> measurements and models according to the four statistical metrics and the 3 atmospheric layers used previously. In the BL, most (5/8) global simulations underestimated the variability of atmospheric CH<sub>4</sub> content ( $\sigma_N$  < 1). On the contrary, regional simulations significantly overestimated this variability with  $\sigma_N$  > 3 for both d01 and d02 domains. Correlation between model products and MAGIC2021 measurements was also found to be low in the BL, no simulations exceeding  $\rho$  = 0.8, with some reaching values below  $\rho$  = 0.4 (PLS NIES a and PLS UoL a). In terms of bias and RMSE, global models had better performance in the BL when compared to regional simulation products, particularly PLS Surf a and b and CAMS v21r1 which all had RMSE<10 ppb and absolute values of bias  $\leq$  1 ppb. Whereas global simulations all displayed a negative bias, both WRF-Chem domains overestimated methane content in the BL, which corresponds to what was observed in the profiles of Figure 7.

The FT was also characterised by an underestimation of variability by global models with most (7/8) having  $\sigma_N < 1$ . Regional simulations along with CAMS *hlkx* once again overestimated variability in that layer, with  $1.7 \le \sigma_N \le 3.5$ . Correlation performance was slightly better than in the BL, with most (6/10) models showing  $\rho > 0.6$ . RMSE and bias performance was also better in the FT than in the BL, with the notable exception of CAMS *hlkx* that displayed a negative bias of  $\sim 30$  ppb as was seen in the profiles of Figure 7.

In the LS, all global models had a similar performance in terms of correlation, achieving the highest values out of the three analysis layers (0.95  $\leq \rho \leq$  0.99). Regional simulations showed a lower correlation with MAGIC2021 measurements, with  $\rho \sim 0.85$  for both domains. Variability was underestimated by all global models in the LS, with  $0.68 \leq \sigma_N \leq 0.95$  while both domains of the regional simulations slightly overestimated variabillity. Positive biases were observed for all simulations in the LS, more particularly for global models which showed 43  $< \overline{\Delta} < 103$  ppb. Regional simulations managed to produce a lower bias, with  $\overline{\Delta} < 10$  ppb for both WRF-Chem d01 and d02. In terms of RMSE, CAMS v21r1 performed best among all global models with RMSE  $\sim 60$  ppb, which aligned with both WRF-Chem domains. For PLS products, the "advanced" physics configuration (b) also showed better results than the "classic" physics scheme (a), both in terms of RMSE and bias.

In conclusion, the evaluation of model simulations against MAGIC2021 CH<sub>4</sub> measurements revealed distinct performance patterns across atmospheric layers. In the BL, global simulations underestimated CH<sub>4</sub> variability and showed lower bias and RMSE compared to regional simulations, which overestimated both variability and CH<sub>4</sub> content. In the FT, regional simulations better represented variability, but correlation remained low for most models, with improved RMSE and bias relative to the BL. In the LS, global models achieved high correlation with MAGIC2021 measurements but displayed large positive biases, while regional simulations provided lower biases and comparable RMSE performance.

# 4.2 Discussion of CH<sub>4</sub> comparisons

450

465

Table 4 shows a comparative assessment of the simulated atmospheric CH<sub>4</sub> content by the 10 modelling frameworks against MAGIC2021 observational data. Consistently with our previous discussion, CAMS *v21r1* shows the best overall performance, in most metrics and layers, having an average rank of 1.75. The table also allows to rank the PLS inversions ensemble according to their average rank in all layers and metrics used (shown in parenthesis): 1. Surf b (3.83), 2. Surf a (4.92), 3. UoL b (5.08), 4. NIES b (5.25), 5. UoL a (7), 6. NIES a (7.58). Thus the worst performing simulations were PLS NIES a and PLS UoL a, with PLS Surf a also performing worst than PLS Surf b. This indicates that updating from the "classic" to "advanced" physics scheme makes a more important difference than a change in observational constraint for these simulations.

We first start by discussing BL positive biases observed in regional WRF-Chem CH<sub>4</sub> products. WRF-Chem d01 and d02 results presented in Figures 7 and 8 are an average over eleven different products for each of d01 and d02 domains. As such, individual products had differing performance scores in the four metrics of the study. To investigate results from regional simulations in more depth, we show results from individual WRF-Chem products in Figure 9. This figure shows the same 4-metric assessment as in Figure 8, but it focuses on individual WRF-Chem simulations, which differ by their input CH<sub>4</sub> emissions from wetlands. WRF-Chem d02 products performed better than d01 in most layers and statistical metrics ( $\rho$  performance was inventory dependent and very close between d01 and d02). For all products, the assessment showed that mixing ratios were

**Table 4.** CH<sub>4</sub> simulations rankings for the three atmospheric layers and the four statistical metrics considered in the study.

		Rank $\sigma_N$	Rank $\rho$	Rank RMSE	Rank $\overline{\Delta}$
CAMC	BL	8	1	5	4
CAMS hlkx	FT	1	1	10	10
	UTLS	10	6	7	7
CAMC	BL	4	3	2	2
CAMS v21r1	FT	4	2	1	1
	UTLS	3	1	2	3
PYVAR-	BL	6	9	8	8
LMDz-SACS	FT	10	6	9	9
NIES a	UTLS	9	3	9	8
PYVAR-	BL	1	7	6	6
LMDz-SACS	FT	9	8	6	6
NIES b	UTLS	6	5	4	5
PYVAR-	BL	3	10	7	7
LMDz-SACS	FT	8	9	8	8
UoL a	UTLS	8	2	10	10
PYVAR-	BL	2	8	4	5
LMDz-SACS	FT	5	10	5	2
UoL b	UTLS	5	4	6	6
PYVAR-	BL	7	6	3	3
LMDz-SACS	FT	7	5	3	3
Surf a	UTLS	7	7	8	9
PYVAR-	BL	5	2	1	1
LMDz-SACS	FT	6	7	7	7
Surf b	UTLS	4	8	5	4
	BL	10	5	10	10
WRF d01	FT	3	4	4	5
	UTLS	2	10	3	2
	BL	9	4	9	9
WRF d02	FT	2	3	2	4
	UTLS	1	9	1	1

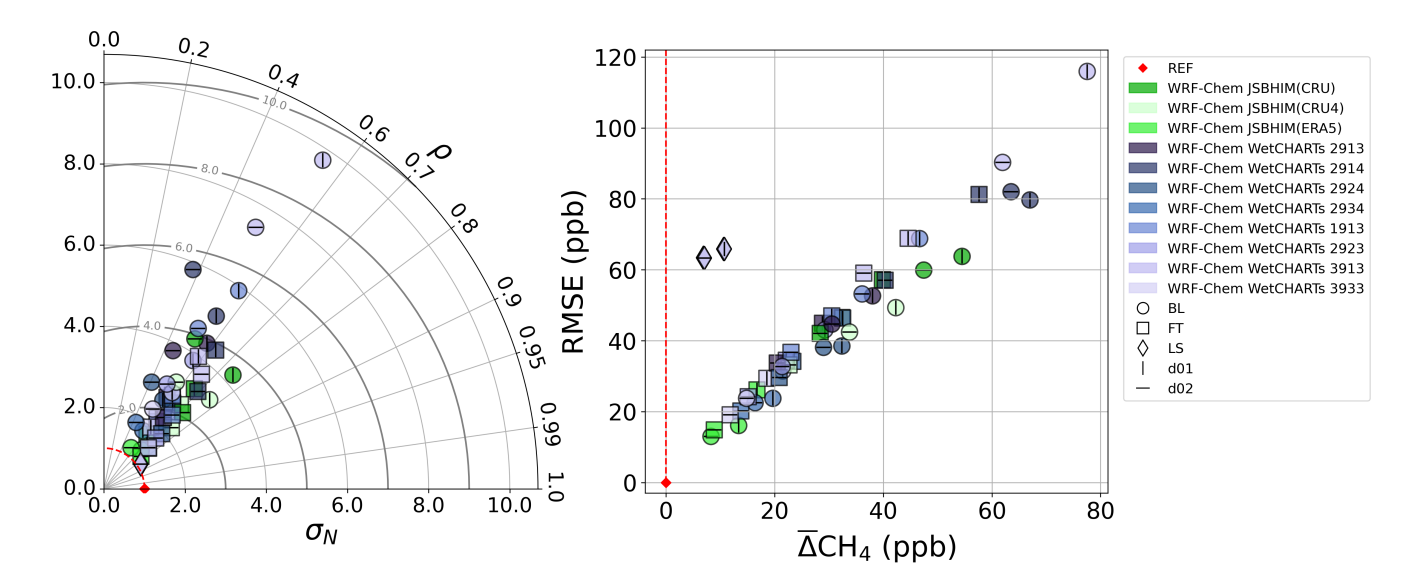


Figure 9. Statistical assessment of individual WRF-Chem simulations against MAGIC2021 measurements Left: Taylor diagram for CH<sub>4</sub> comparison between MAGIC2021 observations and WRF-Chem. The radial axis represents the normalised standard deviation of the modelled CH<sub>4</sub>, whilst angular position represents correlation between modelled and observed CH<sub>4</sub>. Centred RMSE is represented by the radial distance from the reference point. Right: RMSE against bias ( $\overline{\Delta}$ CH<sub>4</sub>) computed from MAGIC2021 observations and modelled CH<sub>4</sub>. RMSE and bias are computed subtracting observed quantities to simulated quantities.

470

475

480

positively biased in the BL and the FT, with a stronger bias in the BL. Most global model products showed a negative bias in the BL (7/8) and an underestimate of variability (5/8), contrary to WRF-Chem mixing ratios which showed both a positive bias and an overestimate of variability. This is consistent with an understimate/overstimate of surface emissions as weak sources would both lead to a negative  $\overline{\Delta}$  and a decrease in variability, whilst overestimated surface emissions would lead to both a positive  $\overline{\Delta}$  and an overstimated variability of boundary layer mixing ratios. This could also be explained by vertical transport issues (e.g. an underestimation of the BL height) in WRF, which could have participated in producing higher CH<sub>4</sub> mixing ratios in the BL. However, the consistency between WRF-Chem simulations and MAGIC2021 data in the FT implies that the vertical transport representation in WRF-Chem was accurate, thus indicating that CH<sub>4</sub> overestimates in the BL from WRF-Chem products was more likely stemming from wetland emission models. This was further confirmed by the relative scale of input emissions shown in Table 1, which correlates with the relative scale of CH<sub>4</sub> overestimates in the BL shown in Figure 9. Moreover, the particular WRF-Chem set-up used in this study has been used in previous studies without showing any issues with BL or FT transport (Lauvaux et al., 2012, 2016). Thus we deduced that inventories overestimated the magnitude of wetland emissions (which could also lead to overestimating flux variability).

These results first showed that low emissions are needed to match observations when looking at averages over the whole MAGIC2021 dataset. Wetland methane releases are typically not homogeneously distributed and continuous in space and time (Rinne et al., 2018; Waletzko and Mitsch, 2014) which makes them hard to fully encompass in inventories. This is reinforced

by the fact that not only WetCHARTs monthly averaged emissions led to such overstimates, but also JSB-HIM products which have a daily time resolution as well as a higher spatial resolution and more complex underlying emission processes. Thus, a true improvement in the representation of wetland emissions would require sub-daily and sub-kilometer resolution as there is no clear difference in performance between monthly/0.5° and daily/0.1° resolution products.

This issue with wetland emission models could be investigated further by combining MAGIC2021 BL observations with high resolution WRF-Chem simulations and other modelling techniques such as Lagrangian particle dispersion modelling.

490

495

500

505

The FT negative bias found between CAMS hlkx and MAGIC2021 observations is similar to previous findings by Membrive et al. (2017) where simulations similar to CAMS hlkx (C-IFS forecast) were compared to a high resolution profile from an AirCore launch in Canada during the StratoScience campaign (CNES - August 2014). More precisely, the instrument (AirCore-HR) was deployed on a stratospheric balloon flight near Timmins, ON. (48.6°N). This study compares well with ours because similar CH<sub>4</sub> sources can be found near both locations, and data was also collected in August. Membrive et al. (2017) found  $\overline{\Delta}$  = -24 ppb when comparing AirCore measurements to the C-IFS forecast. We find an overall tropospheric  $\overline{\Delta}$  of -14.7 ± 16.6 ppb when comparing MAGIC2021 versus CAMS hlkx, which is a comparable result. Further conclusions cannot be drawn from comparing these two studies alone, but this feature is also consistently found when comparing AirCore profiles from AirCore networks (AirCore-Fr, Crevoisier et al. (2023), NOAA; Koffi and Bergamaschi (2018)) with CAMS forecast and analysis products. This suggests the presence of a systematic CH<sub>4</sub> bias in the FT in CAMS forecast and analysis products.

Whilst a significant tropospheric bias was only found between CAMS hlkx and MAGIC2021 measurements, LS analysis highlighted the presence of a strong positive bias for all models (cf. Figure 7). This is particularly important as a stratospheric bias in CH<sub>4</sub> levels affects the performance of models at reproducing the dry-air column-averaged mixing ratio of methane (XCH<sub>4</sub>), which has to be accurately reproduced in order to leverage satellite observations to measure surface emissions of CH<sub>4</sub> (Ostler et al., 2016). To investigate this further, we drew Figure 10 which shows all MAGIC2021 AirCore profiles plotted along with mean and spread of corresponding interpolated model profiles. Measured CH<sub>4</sub> profiles show three distinct phases in the LS. The bottom of the layer is characterised by a first strong gradient, typically from P = 400-300 to P = 200 hPa, which takes CH<sub>4</sub> mixing ratios from their tropospheric average of ~1950 ppb to about 1810 ppb. mixing ratios then remain stable for 100 hPa or less before starting a sharp decrease again in the last layer, between P = 200 and P = 100 hPa. This overall structure is in reality more complex when looking at individual profiles and highlights the stratification of the atmosphere at these altitudes.

Membrive et al. (2017) attribute LS  $\overline{\Delta}>0$  in C-IFS simulations similar to CAMS hlkx to an understimation of the CH<sub>4</sub> stratospheric gradient, which then becomes too steep higher in the stratosphere Verma et al. (2017). We indeed observe a growing positive model bias in the LS between 12 and 20km (or P=200 to P=45 hPa) on the bottom right panel of Figure 7). This bias then decreases and becomes positive for some simulations higher in the stratosphere. These results were found for all global models including CAMS hlkx, which is a similar product to the one assessed in Verma et al. (2017) and Membrive et al. (2017). However, the 4-metric assessment performed on models showed that correlation between MAGIC2021 measurements and all simulations had high correlation in the LS, which indicates a good reproduction of CH<sub>4</sub> gradients by the models within that layer. These results suggest that the CH<sub>4</sub> stratospheric biases found here and in the literature have a complex origin. Figure 10, showed that CH<sub>4</sub> values from AirCores started to decrease more strongly at lower altitudes than in models, meaning

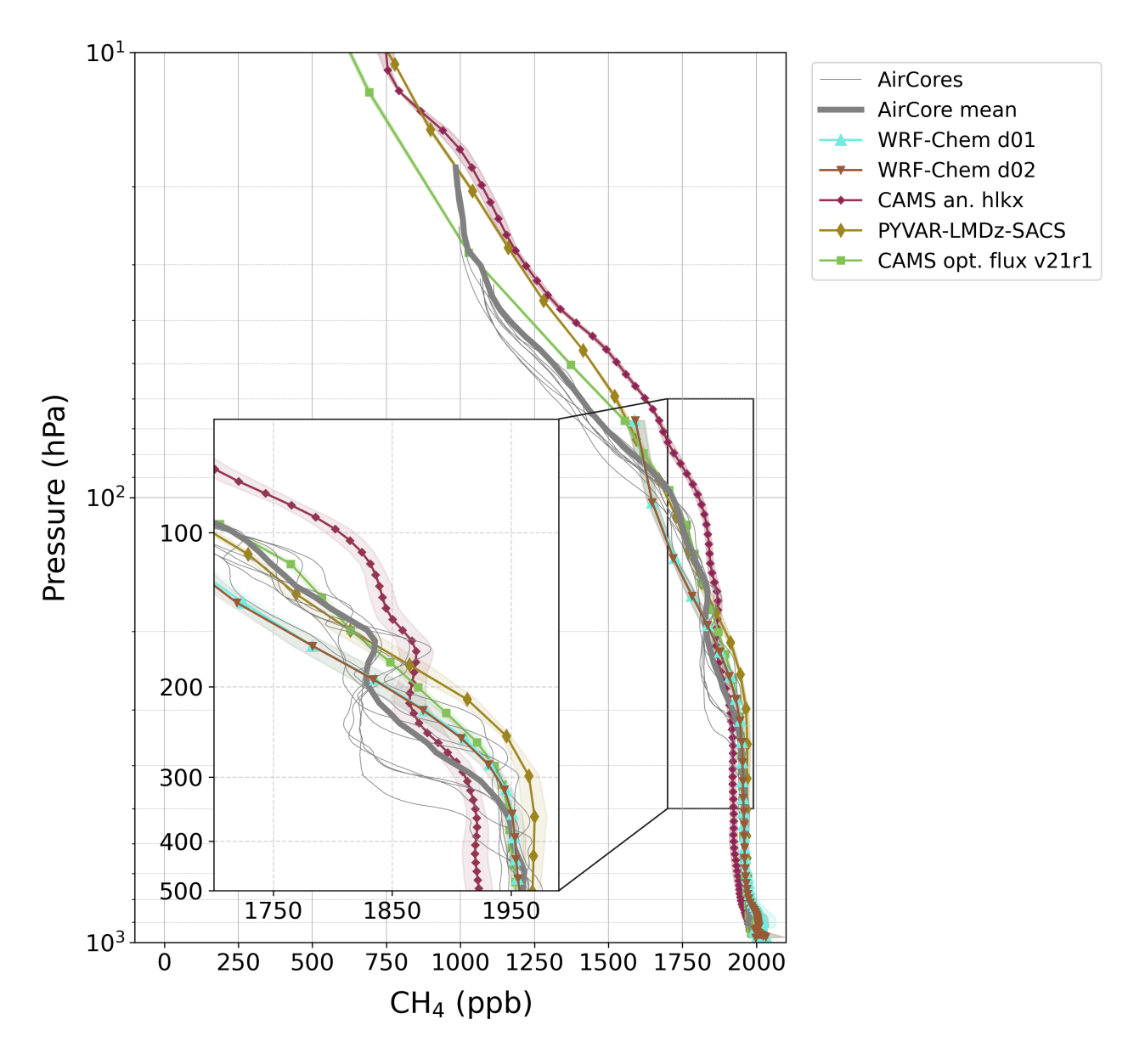


**Figure 10.** CH<sub>4</sub> profiles from MAGIC2021 AirCores (symbol-free lines) plotted with modelled CH<sub>4</sub> profiles (lines with symbols) against pressure. Displayed modelled profiles are averaged over all interpolated profiles for each model and the coloured area represents the  $1-\sigma$  deviation from the mean. From the PLS ensemble, only the best performing product (Surf b) is shown.

that the reduction in CH<sub>4</sub> mixing ratios in the upper troposphere due to interaction with OH radicals could be starting higher in models than in reality. Patra et al. (2011) compared several simulations of CH<sub>4</sub> and CH<sub>3</sub>CCl<sub>3</sub>, including some made with a set-up similar to the PLS model, and showed that models differed in their bias with the same OH field, indicating that other factors than the reaction between CH<sub>4</sub> and tropospheric OH, such as other chemical reactions or transport, are involved. Among the other important chemical reactions, CH<sub>4</sub> is also depleted by chlorine (Cl) in both the troposphere and stratosphere. Thanwerdas et al. (2022) simulated the Cl sink in a CTM also using LMDz for transport and found similar highly positive model biases near the tropopause, on which changes in the Cl field had little to no effect. Together, these results indicate that transport issues in the assessed models are more likely to explain the observed biases than factors related to chemistry.

The strength of CH<sub>4</sub> stratospheric decay has been linked to the rate of stratosphere-troposphere exchanges (STE), which is directly influenced by the Brewer-Dobson circulation (that controls tropopause height tropopause folds) or fronts/cyclones (Holton et al., 1995; Thompson et al., 2014; Locatelli et al., 2015). Modelling STE accurately is therefore crucial to match observed CH<sub>4</sub> mixing ratios at these altitudes because they vary strongly over a short vertical distance depending on the chemical content of the air masses within which measurements are made. Our results regarding tropopause height in temperature profiles (Figure 4) show that outputs from the IFS transport model (which is used in ERA5 and CAMS simulations) have good consistency with observations in the lower stratosphere, indicating that transport issues might be due to other reasons. CAMS *hlkx* has three to four times as many vertical levels as the other products that are compared to MAGIC2021 observations. In the LS, and especially at the tropopause, this feature makes an important difference in terms of structure complexity of profiles. As such, the CAMS *hlkx* bias profile does not show the positive peak of  $\overline{\Delta} \sim 50$ -100 ppb for 300>P>200 hPa that inversion-optimised models (PLS, CAMS *v21r1*) do. This could be because it can capture a more realistic vertical structure of CH<sub>4</sub> depletion near the tropopause, as shown in Figure 10.

Patra et al. (2011); Thompson et al. (2014) showed that STE were poorly modelled in a CTM set-up similar to the PLS simulations used here. This poor performance was attributed to a bad simulation of the Brewer-Dobson circulation, which was too vigorous, inducing too much stratosphere-troposphere mixing. A crucial difference between the set-up from Patra et al. (2011); Thompson et al. (2014) and ours was the number of vertical levels (19 in their set-up versus 39 in ours). Locatelli et al. (2015) have also suggested that more vertical levels would allow for a better modelling of the Brewer-Dobson circulation, notably allowing for a better computation of the tropopause height and better mixing. Their hypothesis, suggesting that a Brewer-Dobson circulation stronger in models than in reality would enhance mixing and reduce the CH<sub>4</sub> gradient at the tropopause fits well with our results, given that the model with the most vertical levels is able to better reproduce observed profile features. Nevertheless, this finding warrants cautious interpretation, as CAMS *hlkx* simulations only display mediocre performance in the lower stratosphere (LS) across our four statistical metrics. The comprehensive summary of our model assessment presented in Table 4 positions CAMS *hlkx* at the 10<sup>th</sup> rank for  $\sigma_N$ , 4<sup>th</sup> for  $\rho$ , and 7<sup>th</sup> for both  $\overline{\Delta}$ CH<sub>4</sub> and RMSE within the LS. It should be noted that CAMS *hlkx* represents a less refined product in relative to other models, lacking surface CH<sub>4</sub> emissions optimisation or data assimilation included in other CAMS products such as CAMS *v21r1*. Potential next steps would involve comparing LS observations with higher vertical resolution emission-optimised CH<sub>4</sub> simulations, thereby enabling more definitive conclusions on this matter.

While we saw that issues with individual chemical species such as OH (Patra et al., 2011) or Cl (Thanwerdas et al., 2022) could not explain the observed CH<sub>4</sub> LS bias by themselves, it is possible that a combination of errors in chemistry modelling could partly explain it. Thus, another possible way to improve the performance of chemistry-transport models in the LS would be to couple them with models that focus on stratospheric chemistry, such as REPROBUS (Lefèvre et al., 1994, 1998; Jourdain et al., 2008), which implement stratospheric chemistry in more detail, notably taking into account more CH<sub>4</sub> sink molecules, thus potentially preventing CH<sub>4</sub> overestimates. Comparing AirCore profiles to LMDz-Reprobus (Marchand et al., 2012) CH<sub>4</sub> products would shed some light on the impact of chemistry on modelled CH<sub>4</sub> mixing ratios in the LS.

# 4.3 Conclusions on CH<sub>4</sub> comparisons

Our model performance intercomparison highlights important differences between MAGIC2021 observations and modelled CH<sub>4</sub> mixing ratios, especially in the LS where all models overestimate atmospheric methane levels. CAMS hlkx analysis showed highest bias of all models in the LS and also suffered from consistent underestimation of atmospheric methane content in the FT. Inversion-optimised products showed better perfomance at every levels than CAMS hlkx. However, CAMS hlkx denser vertical grid at high altitude proved to be a certain advantage to better resolve the structure of CH<sub>4</sub> profiles at the tropopause. Among inversion optimised global chemistry-transport models, CAMS v21r1 showed the best performance in terms of  $\overline{\Delta}$ CH<sub>4</sub>. Standard physics and surface observational constraints were found to be the best combination within the 6 PLS ensemble inversions, this version (Surf b) showing a similar level of performance as CAMS v21r1. We also find that updating the physics scheme from "classic" to "advanced" improves PLS simulations more than a change in observational constraints. Regional simulations were characterised by a strong overestimation of the BL CH<sub>4</sub> atmospheric content, which was not found in global simulations. This overestimation hints toward either an excess in wetland emissions from input bottom-up models or a vertical transport problem in WRF-Chem. The good correspondance between WRF-Chem simulations and MAGIC2021 data in the FT indicate that the issue probably lies with wetland emission models rather than with the vertical transport representation in WRF-Chem.

# 5 Conclusions

565

575

580

585

ERA5 reanalysis and WRF simulations were assessed using meteorological data from MAGIC2021. Methane in-situ measurements from MAGIC2021 were also exploited to assess atmospheric composition models: the analysis product CAMS *hlkx*, the inversion-optimised product CAMS *v21r1*, six PYVAR-LMDz-SACS (PLS) ensemble inversions and WRF-Chem regional simulations. Over the six days of MAGIC2021, meteorological data from ERA5 showed better agreement with observations than WRF on average, due to both data assimilation and lower resolution that enhance performance in such an exercise. WRF performance was however very close for all physical quantities assessed, which gives us confidence in its ability to simulate regional atmospheric physics for MAGIC2021. Among global simulations, inversion-optimised simulations of CH<sub>4</sub> mixing ratios performed best, especially close to the surface. CAMS *v21r1* showed slightly better performance than the best product from the PLS ensemble inversions. A detailed analysis of regional simulations with WRF-Chem was performed, revealing

perfomance disparities among CH<sub>4</sub> products. Notably, near-neutral to strongly positive biases were observed in the boundary layer, indicating a tendency of wetland emission models to overestimate CH<sub>4</sub> emissions, at least for the limited region and timeframe captured by the observations. CH<sub>4</sub> profiles were also characterised by performance discrepancies near the tropopause, where CH<sub>4</sub> content is depleted mainly by its reaction with OH radicals, and can also be affected by stratospheric intrusions. All models showed a delayed vertical gradient of CH<sub>4</sub> mixing ratios near the tropopause, leading to a positive bias in the stratosphere. Comparisons with CAMS hlkx showed that high vertical resolution allows to better capture vertical structure of CH<sub>4</sub> profiles in the stratosphere, with a large overestimate still. These results call for more work dedicated to improve the transport and chemistry of models in the LS, which could be done by separate stratosphere models, specialised in the task. Finally, we aknowledge that the MAGIC2021 dataset is limited in both spatial and temporal extents, limiting its ability to fully assess models. While the MAGIC2021 campaign provides valuable observations, supplementing this with additional datasets could offer a more comprehensive evaluation of model performance. This could be partly addressed by using data from other campaigns (e.g. CoMet 2.0 campaign over Canada in the summer of 2022, (DLR, 2022)) together with data from MAGIC2021. Still the results presented here represent a rare opportunity to assess the performance of models against a large, high resolution dataset, and over an area where few measurements are usually taken, highlighting the ability of extended campaigns at high latitudes to characterise local processes. More frequent campagins could allow to extend this kind of performance assessment of global and regional models to other circumpolar regions and seasons, while also allowing a long term tracking of atmospheric composition changes in the Arctic.

590

595

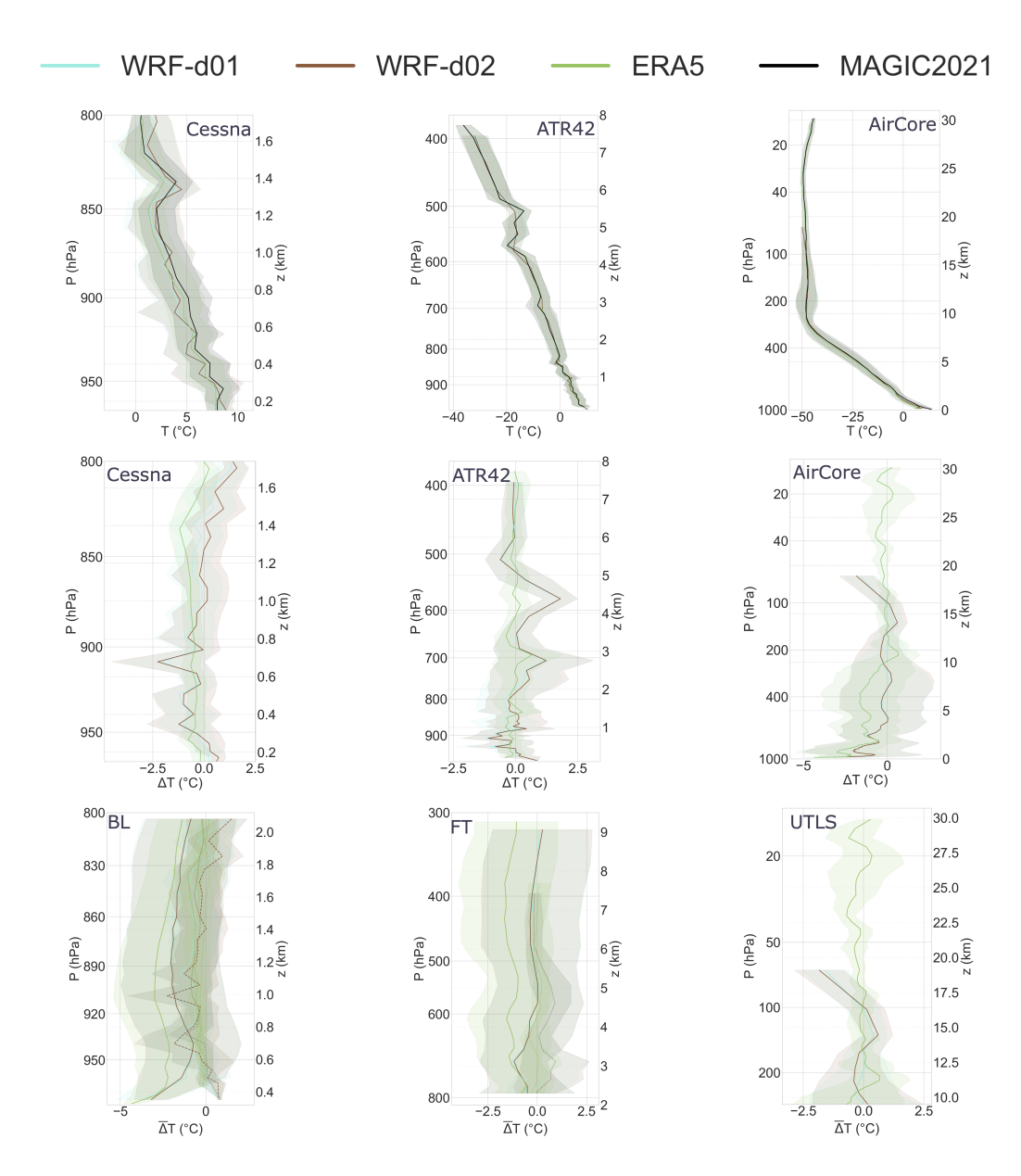


**Figure A1.** Temperature intercomparison between MAGIC2021 data and weather models. Profiles are computed using full weather balloon dataset and profile sections of ATR42 and Cessna flights. ERA5 related profiles are shown in green, WRF d01 in blue and WRF d02 in red. **Top:** Mean temperature profiles accross all flights from each platform (black) plotted with modelled temperatures interpolated on platform trajectories: Cessna (left), ATR42 (centre) and weather balloon (right). **Middle:** Temperature bias profile between for each platform: Cessna (left), ATR42 (centre) and weather balloon (right). **Bottom:** Sections of temperature bias profiles correponding to the 3 analysis levels: BL (left), FT (centre) and LS (right), where Cessna data is shown in dashed lines, ATR42 data in dotted lines and AirCore data in solid lines. Shaded areas represent the 1-σ deviation from the mean temperature or temperature bias profiles.

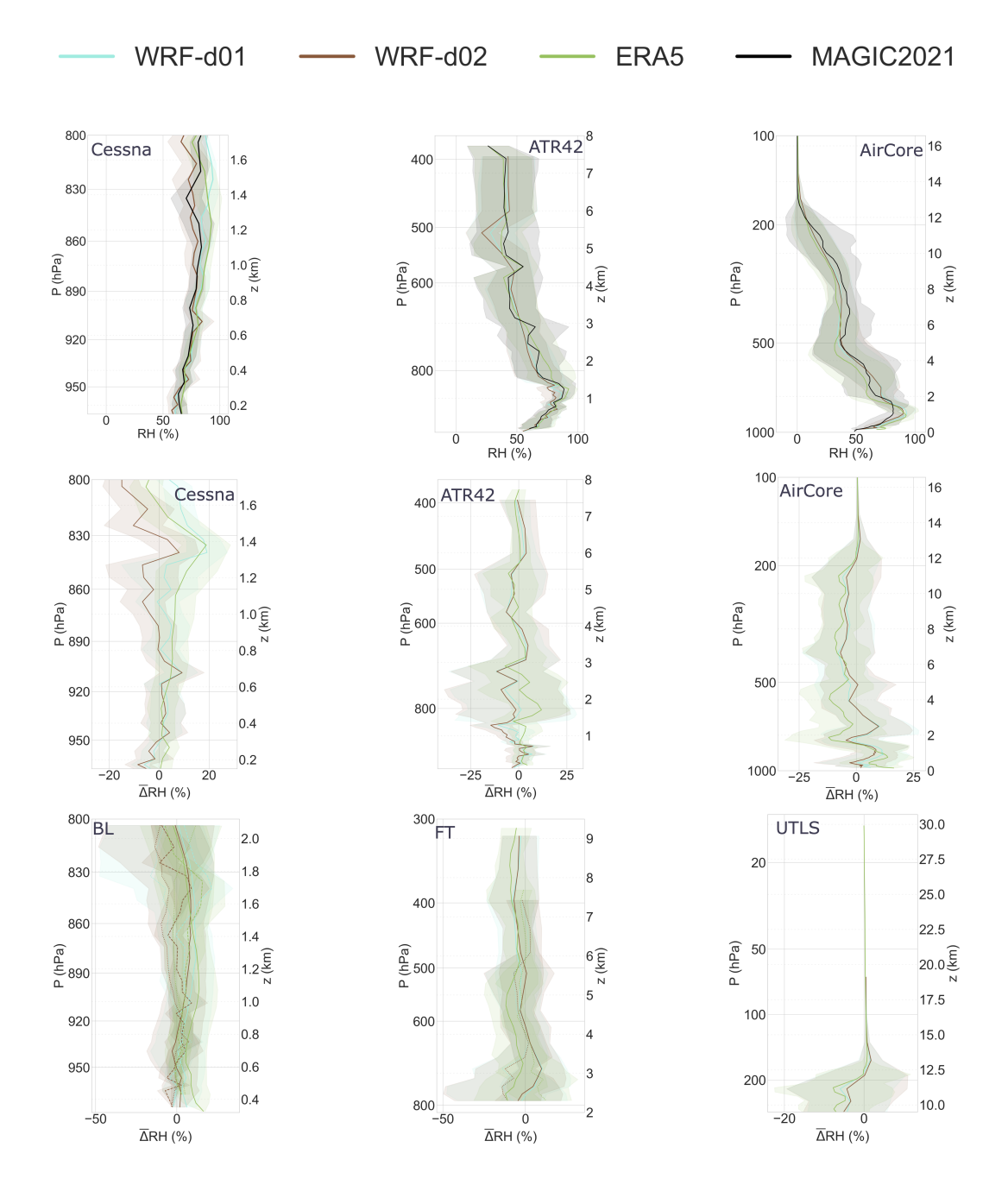


**Figure A2.** RH intercomparison between MAGIC2021 data and weather models. Profiles are computed using full weather balloon dataset and profile sections of ATR42 and Cessna flights. ERA5 related profiles are shown in green, WRF d01 in blue and WRF d02 in red. **Top:** Mean RH profiles accross all flights from each platform (black) plotted with modelled RH interpolated on platform trajectories: Cessna (left), ATR42 (centre) and weather balloon (right). **Middle:** RH bias profile for each platform: Cessna (left), ATR42 (centre) and weather balloon (right). **Bottom:** Sections of RH bias profiles correponding to the 3 analysis levels: BL (left), FT (centre) and LS (right), where Cessna data is shown in dashed lines, ATR42 data in dotted lines and AirCore data in solid lines. Shaded areas represent the 1-σ deviation from the mean RH or RH bias profiles.

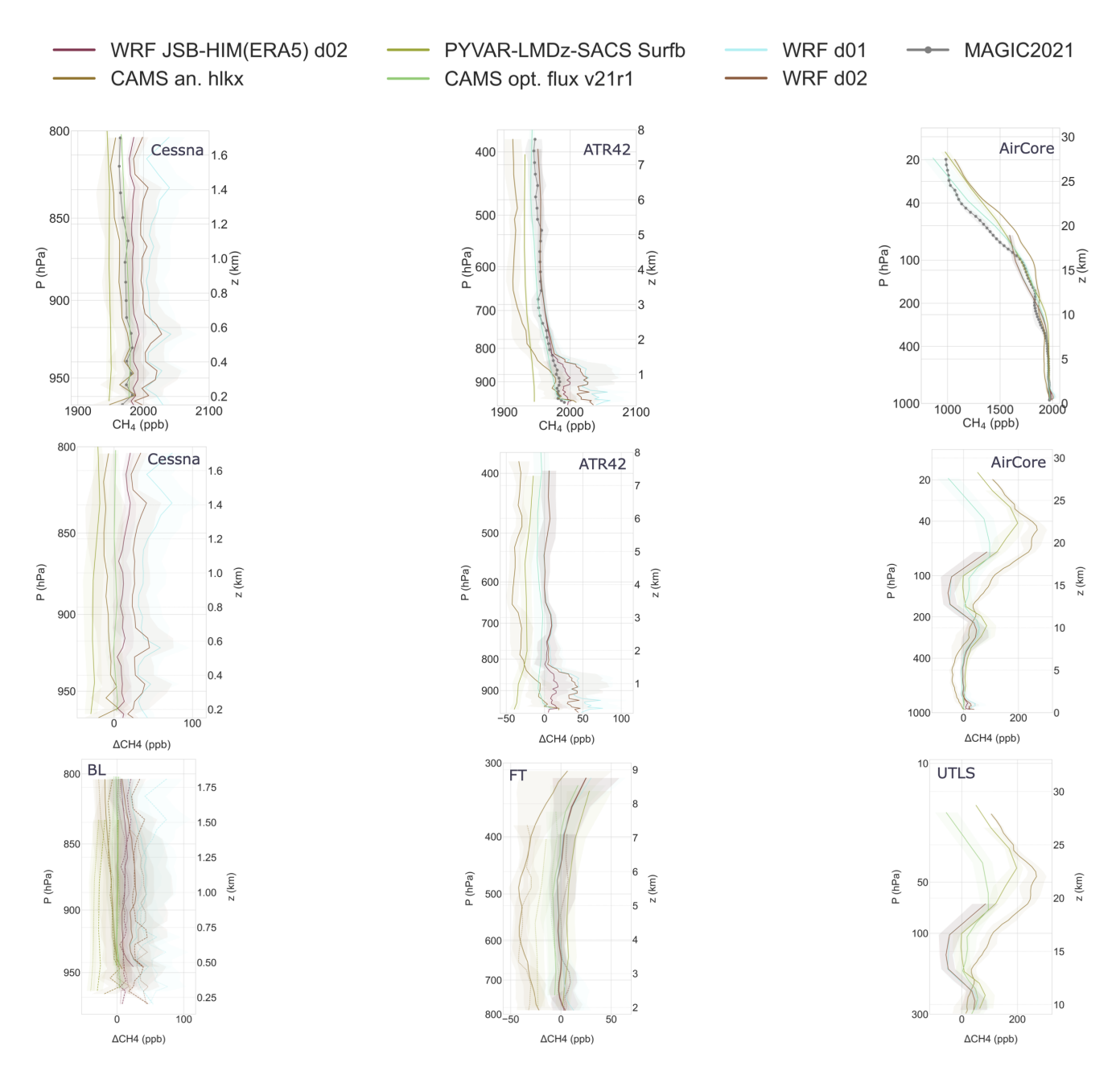


**Figure A3.** Methane intercomparison between MAGIC2021 data and chemistry-transport models. Profiles are computed using the full AirCore dataset and profile sections of ATR42 and Cessna flights. **Top:** Mean CH<sub>4</sub> profiles accross all flights from each platform (dotted grey line) plotted with modelled CH<sub>4</sub> interpolated on platform trajectories: Cessna (left), ATR42 (centre) and weather balloon (right). **Middle:**CH<sub>4</sub> bas profile for each platform: Cessna (left), ATR42 (centre) and weather balloon (right). **Bottom:** Sections of CH<sub>4</sub> bias profiles correponding to the 3 analysis levels: BL (left), FT (centre) and LS (right), where Cessna data is shown in dashed lines, ATR42 data in dotted lines and AirCore data in solid lines. Shaded areas represent the 1-σ deviation from the mean CH<sub>4</sub> or CH<sub>4</sub> bias profiles.

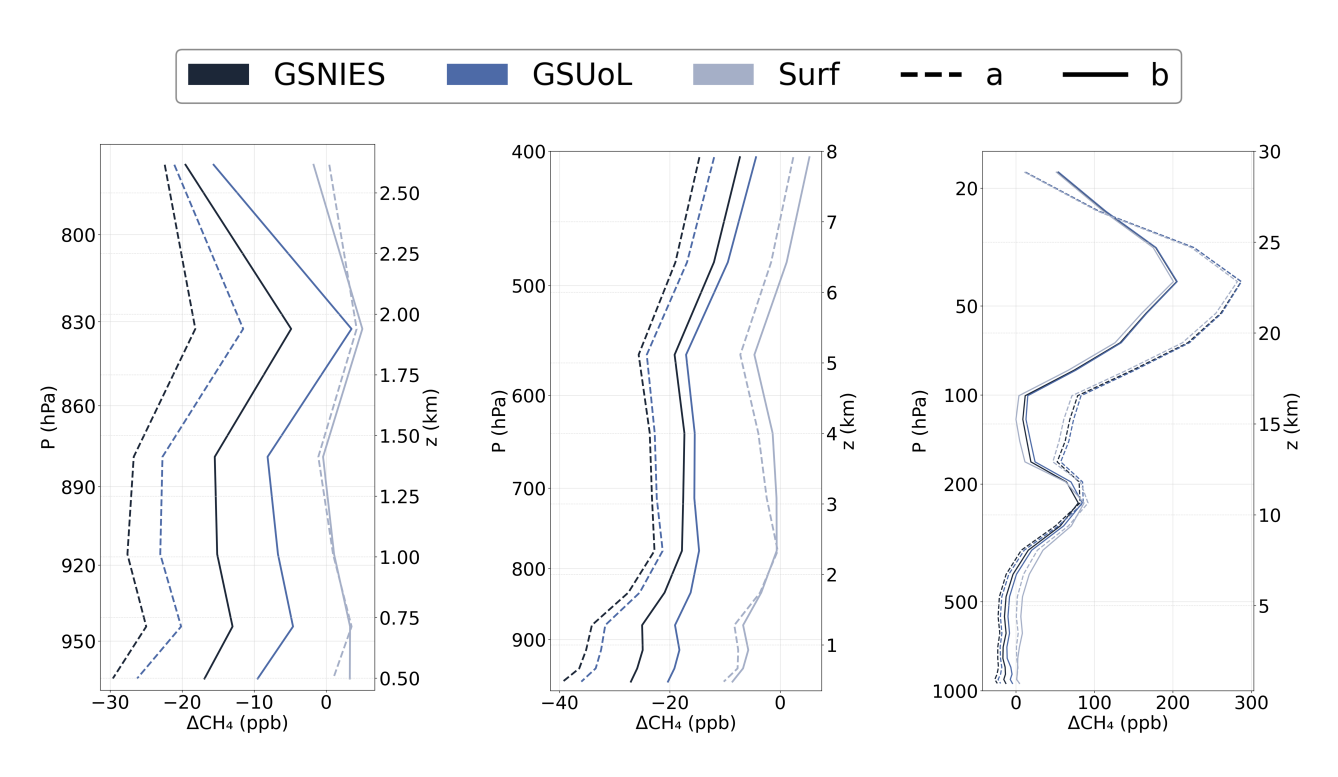


**Figure A4.** Mean PYVAR-LMDz-SACS bias from all 6 configurations computed with MAGIC2021 data: Cessna (left), ATR42 (middle) and AirCore (right) measurements.

Data availability. Data from MAGIC2021 will be available on the French national center for Atmospheric data and services AERIS catalogue, and on the HALO (Re3data.Org, 2016) database. WRF-Chem simulations outputs are available upon request.

Author contributions. - FL & CC designed the study

- FL performed the comparisons between MAGIC2021 data and model outputs
- ERA5, CAMS hlkx and CAMS v21r1 data was retrieved by JP
- WRF-Chem simulations were designed and run by FL with support from TL and CA
- 610 MS and XL provided the PYVAR-LMDz-SACS ensemble data
  - Weather balloon data were acquired by AG, JM and were processed by JP and TP
  - ATR42 CH<sub>4</sub> data were calibrated by MR and processed by AG and FL
  - Cessna data were acquired and provided by AF, K-DG, AR as well as Heidi Huntrieser, Vladyslav Nenakhov and Magdalena Pühl
  - Cessna meteorological data was produced by Vladyslav Nenakhov
- 615 Cessna CH<sub>4</sub> data was produced by AF

620

625

- Analysis of results was done by FL with support from all co-authors

Competing interests. The authors declare that they have no conflict of interest.

Acknowledgements. We thank CNRS MITI for funding this research as well as CNRS, CNES, EUMETSAT and ESA for funding MAGIC2021. This study also benefited from the IPSL Data and Computing Center ESPRI which is supported by CNRS, SU, CNES and Ecole Polytechnique, as well as the ROMEO HPC center at the University of Reims Champagne-Ardenne. T. Lauvaux was supported by the French fellowship Make Our Planet Great Again (CIUDAD, CNRS), the French Ministry of Research (Junior Chair professor CASAL) and the European Space Agency (project MethaneWatch).

Carbon footprint. The full carbon footprint of the MAGIC2021 campaign is still being estimated. For this study, we compute an approximate value based on the highest emitters: aircraft flights. The Cessna from DLR has a 675HP turbine engine and flew for 27h22min, which according to Labos1point5 data equates to an emissions of  $13 \pm 1$  tCO<sub>2</sub>. The ATR42 from SAFIRE has a 3800HP turbine engine and flew for 25h22min, which equates to emissions of  $32 \pm 2$  tCO<sub>2</sub>. Therefore the total carbon footprint of aircraft flights associated to this paper is  $45 \pm 2$  tCO<sub>2</sub>. The balloon's carbon footprint is more complicated to estimate. Most recoveries were performed using a helicopter for which engine and flight time data were not part of the MAGIC2021 dataset, resulting in a lack of information. Additionally, the helium used to inflate campaign balloons is a potent greenhouse gas that is released in the high troposphere/lower stratosphere everytime a balloon is used. Working out the full carbon footprint of radiosoundings therefore requires converting released helium to CO<sub>2</sub> equivalent which has not yet been done for MAGIC2021. The carbon footprint of campaign measurements involved in the study presented here is therefore not complete, and probably totals to more than 50 tCO<sub>2</sub>. The campaign as a whole will have a higher carbon footprint still, as it includes the footprint of

meals provided during the campaign, travels to Kiruna for every team, additional airborne measurements that were not used in this paper, as well as tools, clothes and instruments that were bought especially for MAGIC2021. Also neglected here is the footprint of the data analysis and model simulations post-campaign, which are run using high performance computing facilities. Carbon footprint numbers given here are therefore neither representative of the whole campaign nor of the data analysis and modelling footprint, so it should be considered as a lower bound for the footprint of this paper only.

## References

645

660

- Alto, T.: VERIFY Observation-based System for Monitoring and Verification of Greenhouse Gases D4.4, Tech. rep., 2019.
  - Agustí-Panareda, A., Barré, J., Massart, S., Inness, A., Aben, I., Ades, M., Baier, B. C., Balsamo, G., Borsdorff, T., Bousserez, N., Boussetta, S., Buchwitz, M., Cantarello, L., Crevoisier, C., Engelen, R., Eskes, H., Flemming, J., Garrigues, S., Hasekamp, O., Huijnen, V., Jones, L., Kipling, Z., Langerock, B., McNorton, J., Meilhac, N., Noël, S., Parrington, M., Peuch, V.-H., Ramonet, M., Razinger, M., Reuter, M., Ribas, R., Suttie, M., Sweeney, C., Tarniewicz, J., and Wu, L.: Technical Note: The CAMS Greenhouse Gas Reanalysis from 2003 to 2020, Atmospheric Chemistry and Physics, 23, 3829–3859, https://doi.org/10.5194/acp-23-3829-2023, 2023.
  - Ahlenius, H.: Permafrost Extent in the Northern Hemisphere | GRID-Arendal, 2016.
  - AMAP: Arctic Climate Change Update 2021: Key Trends and Impacts, Summary for Policy makers, Arctic Monitoring and Assessment Programme (AMAP), Oslo, Norway, 2021.
- Bergamaschi, P., Krol, M., Dentener, F., Vermeulen, A., Meinhardt, F., Graul, R., Ramonet, M., Peters, W., and Dlugokencky, E. J.: Inverse Modelling of National and European CH4 Emissions Using the Atmospheric Zoom Model TM5, Atmos. Chem. Phys., p. 30, 2005.
  - Bergamaschi, P., Frankenberg, C., Meirink, J. F., Krol, M., Villani, M. G., Houweling, S., Dentener, F., Dlugokencky, E. J., Miller, J. B., Gatti, L. V., Engel, A., and Levin, I.: Inverse Modeling of Global and Regional CH4 Emissions Using SCIAMACHY Satellite Retrievals, Journal of Geophysical Research: Atmospheres, 114, https://doi.org/10.1029/2009JD012287, 2009.
- Bloom, A. A., Bowman, K. W., Lee, M., Turner, A. J., Schroeder, R., Worden, J. R., Weidner, R., McDonald, K. C., and Jacob, D. J.: A

  Global Wetland Methane Emissions and Uncertainty Dataset for Atmospheric Chemical Transport Models (WetCHARTs Version 1.0),

  Geoscientific Model Development, 10, 2141–2156, https://doi.org/10.5194/gmd-10-2141-2017, 2017.
  - Booth, A., Goodwin, P., and Cael, B. B.: Ice Sheet-Albedo Feedback Estimated From Most Recent Deglaciation, Geophysical Research Letters, 51, e2024GL109 953, https://doi.org/10.1029/2024GL109953, 2024.
  - Brühl, C. and Crutzen, P. J.: MPIC Two-dimensional Model, in: The Atmospheric Effects of Stratospheric Aircraft: Report of the 1992 Models and Measurements Workshop, vol. 1 of *NASA Reference Publications*, NASA, 1993.
    - Bullock, O. R., Alapaty, K., Herwehe, J. A., Mallard, M. S., Otte, T. L., Gilliam, R. C., and Nolte, C. G.: An Observation-Based Investigation of Nudging in WRF for Downscaling Surface Climate Information to 12-Km Grid Spacing, https://doi.org/10.1175/JAMC-D-13-030.1, 2014.
    - C3S: ERA5 Hourly Data on Single Levels from 1940 to Present, https://doi.org/10.24381/CDS.ADBB2D47, 2018.
- 665 Crevoisier, C.: MAGIC2021 Logbook, https://magic.aeris-data.fr/magic2021/, 2021.
  - Crevoisier, C., Pernin, J., Colomb, A., Joly, L., and Ramonet, M.: AirCore-Fr Dataset Catalogue, 2023.
  - Díaz-Isaac, L. I., Lauvaux, T., and Davis, K. J.: Impact of Physical Parameterizations and Initial Conditions on Simulated Atmospheric Transport and CO<sub>2</sub> Mole Fractions in the US Midwest, Atmospheric Chemistry and Physics, 18, 14813–14835, https://doi.org/10.5194/acp-18-14813-2018, 2018.
- 670 DLR: CoMet 2.0 Arctic Research Campaign on Greenhouse Gases in the High Latitudes, 2022.
  - Emanuel, K. A.: A Scheme for Representing Cumulus Convection in Large-Scale Models, Journal of the Atmospheric Sciences, 48, 2313–2329, https://doi.org/10.1175/1520-0469(1991)048<2313:ASFRCC>2.0.CO;2, 1991.
  - Eugenio, R. G. and Macalalad, E. P.: Monthly Observations of Cold-point Tropopause Temperature and Height for 2008 in the Philippines Using COSMIC GPS Radio Occultations, Journal of Physics: Conference Series, 1936, 012 019, https://doi.org/10.1088/1742-6596/1936/1/012019, 2021.

- European Environment Agency: CORINE Land Cover 2018 (Raster 100 m), Europe, 6-Yearly Version 2020\_20u1, May 2020, https://doi.org/10.2909/960998C1-1870-4E82-8051-6485205EBBAC, 2019.
- Feng, S., Lauvaux, T., Davis, K. J., Keller, K., Zhou, Y., Williams, C., Schuh, A. E., Liu, J., and Baker, I.: Seasonal Characteristics of Model Uncertainties From Biogenic Fluxes, Transport, and Large-Scale Boundary Inflow in Atmospheric CO2 Simulations Over North America, Journal of Geophysical Research: Atmospheres, 124, 14325–14346, https://doi.org/10.1029/2019JD031165, 2019.
- Fiehn, A., Kostinek, J., Eckl, M., Klausner, T., Gałkowski, M., Chen, J., Gerbig, C., Röckmann, T., Maazallahi, H., Schmidt, M., Korbeń, P., Neçki, J., Jagoda, P., Wildmann, N., Mallaun, C., Bun, R., Nickl, A.-L., Jöckel, P., Fix, A., and Roiger, A.: Estimating CH<Sub&gt;4&lt;/Sub&gt;, CO&lt;Sub&gt;2&lt;/Sub&gt; and CO Emissions from Coal Mining and Industrial Activities in the Upper Silesian Coal Basin Using an Aircraft-Based Mass Balance Approach, Atmospheric Chemistry and Physics, 20, 12675–12695, https://doi.org/10.5194/acp-20-12675-2020, 2020.
- Gómez-Navarro, J. J., Raible, C. C., and Dierer, S.: Sensitivity of the WRF Model to PBL Parametrisations and Nesting Techniques: Evaluation of Wind Storms over Complex Terrain, Geoscientific Model Development, 8, 3349–3363, https://doi.org/10.5194/gmd-8-3349-2015, 2015.
- Grandpeix, J.-Y., Lafore, J.-P., and Cheruy, F.: A Density Current Parameterization Coupled with Emanuel's Convection Scheme. Part II: 1D Simulations, Journal of the Atmospheric Sciences, 67, 898–922, https://doi.org/10.1175/2009JAS3045.1, 2010.
  - Grell, G. A. and Dévényi, D.: A Generalized Approach to Parameterizing Convection Combining Ensemble and Data Assimilation Techniques, Geophysical Research Letters, 29, 38–1–38–4, https://doi.org/10.1029/2002GL015311, 2002.
  - Hall, A.: The Role of Surface Albedo Feedback in Climate, 2004.

680

- Hall, B. D., Crotwell, A. M., Kitzis, D. R., Mefford, T., Miller, B. R., Schibig, M. F., and Tans, P. P.: Revision of the World Meteorological
   Organization Global Atmosphere Watch (WMO/GAW) CO<sub>2</sub> Calibration Scale, Atmospheric Measurement Techniques, 14, 3015–3032,
   https://doi.org/10.5194/amt-14-3015-2021, 2021.
  - Hersbach, H., Bell, B., Berrisford, P., Hirahara, S., Horányi, A., Muñoz-Sabater, J., Nicolas, J., Peubey, C., Radu, R., Schepers, D., Simmons, A., Soci, C., Abdalla, S., Abellan, X., Balsamo, G., Bechtold, P., Biavati, G., Bidlot, J., Bonavita, M., De Chiara, G., Dahlgren, P., Dee, D., Diamantakis, M., Dragani, R., Flemming, J., Forbes, R., Fuentes, M., Geer, A., Haimberger, L., Healy, S., Hogan, R. J.,
- Hólm, E., Janisková, M., Keeley, S., Laloyaux, P., Lopez, P., Lupu, C., Radnoti, G., de Rosnay, P., Rozum, I., Vamborg, F., Villaume, S., and Thépaut, J.-N.: The ERA5 Global Reanalysis, Quarterly Journal of the Royal Meteorological Society, 146, 1999–2049, https://doi.org/10.1002/qj.3803, 2020.
  - Holton, J. R., Haynes, P. H., McIntyre, M. E., Douglass, A. R., Rood, R. B., and Pfister, L.: Stratosphere-Troposphere Exchange, Reviews of Geophysics, 33, 403–439, https://doi.org/10.1029/95RG02097, 1995.
- Hong, S.-Y., Dudhia, J., and Chen, S.-H.: A Revised Approach to Ice Microphysical Processes for the Bulk Parameterization of Clouds and Precipitation, Monthly Weather Review, 132, 103–120, https://doi.org/10.1175/1520-0493(2004)132<0103:ARATIM>2.0.CO;2, 2004.
  - Houweling, S., Dentener, F., and Lelieveld, J.: The Impact of Nonmethane Hydrocarbon Compounds on Tropospheric Photochemistry, Journal of Geophysical Research: Atmospheres, 103, 10 673–10 696, https://doi.org/10.1029/97JD03582, 1998.
- Iacono, M. J., Delamere, J. S., Mlawer, E. J., Shephard, M. W., Clough, S. A., and Collins, W. D.: Radiative Forcing by Long-Lived
   Greenhouse Gases: Calculations with the AER Radiative Transfer Models, Journal of Geophysical Research: Atmospheres, 113, https://doi.org/10.1029/2008JD009944, 2008.
  - Jammalamadaka, S. R. and Sengupta, A.: Topics in Circular Statistics, no. v. 5 in Series on Multivariate Analysis, World Scientific, River Edge, N.J, 2001.

- Jansen, E., Christensen, J. H., Dokken, T., Nisancioglu, K. H., Vinther, B. M., Capron, E., Guo, C., Jensen, M. F., Langen, P. L., Pedersen,
- R. A., Yang, S., Bentsen, M., Kjær, H. A., Sadatzki, H., Sessford, E., and Stendel, M.: Past Perspectives on the Present Era of Abrupt Arctic Climate Change, Nature Climate Change, 10, 714–721, https://doi.org/10.1038/s41558-020-0860-7, 2020.
  - Jiménez, P. A., Dudhia, J., González-Rouco, J. F., Navarro, J., Montávez, J. P., and García-Bustamante, E.: A Revised Scheme for the WRF Surface Layer Formulation, Monthly Weather Review, 140, 898–918, https://doi.org/10.1175/MWR-D-11-00056.1, 2012.
- Johnson, M. S., Matthews, E., Du, J., Genovese, V., and Bastviken, D.: Methane Emission From Global Lakes: New Spatiotemporal Data and Observation-Driven Modeling of Methane Dynamics Indicates Lower Emissions, Journal of Geophysical Research: Biogeosciences, 127, e2022JG006793, https://doi.org/10.1029/2022JG006793, 2022.
  - Jourdain, L., Bekki, S., Lott, F., and Lefèvre, F.: The Coupled Chemistry-Climate Model LMDz-REPROBUS: Description and Evaluation of a Transient Simulation of the Period 1980–1999, Annales Geophysicae, 26, 1391–1413, https://doi.org/10.5194/angeo-26-1391-2008, 2008.
- Kain, J. S.: The Kain–Fritsch Convective Parameterization: An Update, Journal of Applied Meteorology and Climatology, 43, 170–181, https://doi.org/10.1175/1520-0450(2004)043<0170:TKCPAU>2.0.CO;2, 2004.
  - Kaiser, J. W., Heil, A., Andreae, M. O., Benedetti, A., Chubarova, N., Jones, L., Morcrette, J.-J., Razinger, M., Schultz, M. G., Suttie, M., and van der Werf, G. R.: Biomass Burning Emissions Estimated with a Global Fire Assimilation System Based on Observed Fire Radiative Power, Biogeosciences, 9, 527–554, https://doi.org/10.5194/bg-9-527-2012, 2012.
- 730 Karion, A., Sweeney, C., Tans, P., and Newberger, T.: AirCore: An Innovative Atmospheric Sampling System, Journal of Atmospheric and Oceanic Technology, 27, 1839–1853, https://doi.org/10.1175/2010JTECHA1448.1, 2010.
  - Kärnä, T. and Baptista, A. M.: Evaluation of a Long-Term Hindcast Simulation for the Columbia River Estuary, Ocean Modelling, 99, 1–14, https://doi.org/10.1016/j.ocemod.2015.12.007, 2016.
  - Koffi, E. and Bergamaschi, P.: Evaluation of Copernicus Atmosphere Monitoring Service Methane Products., Publications Office, LU, 2018.
- 735 Lauvaux, T.: Psu-Inversion/WRF boundary coupling, Penn State Inversion working group, 2022.
  - Lauvaux, T., Schuh, A. E., Uliasz, M., Richardson, S., Miles, N., Andrews, A. E., Sweeney, C., Diaz, L. I., Martins, D., Shepson, P. B., and Davis, K. J.: Constraining the CO<sub>2</sub> Budget of the Corn Belt: Exploring Uncertainties from the Assumptions in a Mesoscale Inverse System, Atmospheric Chemistry and Physics, 12, 337–354, https://doi.org/10.5194/acp-12-337-2012, 2012.
  - Lauvaux, T., Miles, N. L., Deng, A., Richardson, S. J., Cambaliza, M. O., Davis, K. J., Gaudet, B., Gurney, K. R., Huang, J., O'Keefe, D.,
- Song, Y., Karion, A., Oda, T., Patarasuk, R., Razlivanov, I., Sarmiento, D., Shepson, P., Sweeney, C., Turnbull, J., and Wu, K.: High-Resolution Atmospheric Inversion of Urban CO2 Emissions during the Dormant Season of the Indianapolis Flux Experiment (INFLUX), Journal of Geophysical Research: Atmospheres, 121, 5213–5236, https://doi.org/10.1002/2015JD024473, 2016.
  - Lawrence, M. G., Jöckel, P., and von Kuhlmann, R.: What Does the Global Mean OH Concentration Tell Us?, Atmospheric Chemistry and Physics, 1, 37–49, https://doi.org/10.5194/acp-1-37-2001, 2001.
- Lefèvre, F., Brasseur, G. P., Folkins, I., Smith, A. K., and Simon, P.: Chemistry of the 1991–1992 Stratospheric Winter: Three-dimensional Model Simulations, Journal of Geophysical Research: Atmospheres, 99, 8183–8195, https://doi.org/10.1029/93JD03476, 1994.
  - Lefèvre, F., Figarol, F., Carslaw, K. S., and Peter, T.: The 1997 Arctic Ozone Depletion Quantified from Three-Dimensional Model Simulations, Geophysical Research Letters, 25, 2425–2428, https://doi.org/10.1029/98GL51812, 1998.
- Li, M., Karu, E., Brenninkmeijer, C., Fischer, H., Lelieveld, J., and Williams, J.: Tropospheric OH and Stratospheric OH and Cl Concentrations Determined from CH4, CH3Cl, and SF6 Measurements, npj Climate and Atmospheric Science, 1, 1–7, https://doi.org/10.1038/s41612-018-0041-9, 2018.

- Lin, X., Peng, S., Ciais, P., Hauglustaine, D., Lan, X., Liu, G., Ramonet, M., Xi, Y., Yin, Y., Zhang, Z., Bösch, H., Bousquet, P., Chevallier, F., Dong, B., Gerlein-Safdi, C., Halder, S., Parker, R. J., Poulter, B., Pu, T., Remaud, M., Runge, A., Saunois, M., Thompson, R. L., Yoshida, Y., and Zheng, B.: Recent Methane Surges Reveal Heightened Emissions from Tropical Inundated Areas, Nature Communications, 15, 10 894, https://doi.org/10.1038/s41467-024-55266-y, 2024.
  - Locatelli, R., Bousquet, P., Hourdin, F., Saunois, M., Cozic, A., Couvreux, F., Grandpeix, J.-Y., Lefebvre, M.-P., Rio, C., Bergamaschi, P., Chambers, S. D., Karstens, U., Kazan, V., van der Laan, S., Meijer, H. a. J., Moncrieff, J., Ramonet, M., Scheeren, H. A., Schlosser, C., Schmidt, M., Vermeulen, A., and Williams, A. G.: Atmospheric Transport and Chemistry of Trace Gases in LMDz5B: Evaluation and Implications for Inverse Modelling, Geoscientific Model Development, 8, 129–150, https://doi.org/10.5194/gmd-8-129-2015, 2015.
- 760 Louis, J.-F.: A Parametric Model of Vertical Eddy Fluxes in the Atmosphere, Boundary-Layer Meteorology, 17, 187–202, https://doi.org/10.1007/BF00117978, 1979.
  - MacDougall, A. H.: Estimated Effect of the Permafrost Carbon Feedback on the Zero Emissions Commitment to Climate Change, Biogeosciences, 18, 4937–4952, https://doi.org/10.5194/bg-18-4937-2021, 2021.
- Mallaun, C., Giez, A., and Baumann, R.: Calibration of 3-D Wind Measurements on a Single-Engine Research Aircraft, Atmospheric Measurement Techniques, 8, 3177–3196, https://doi.org/10.5194/amt-8-3177-2015, 2015.
  - Marchand, M., Keckhut, P., Lefebvre, S., Claud, C., Cugnet, D., Hauchecorne, A., Lefèvre, F., Lefebvre, M. P., Jumelet, J., Lott, F., Hourdin, F., Thuillier, G., Poulain, V., Bossay, S., Lemennais, P., David, C., and Bekki, S.: Dynamical Amplification of the Stratospheric Solar Response Simulated with the Chemistry-Climate Model LMDz-Reprobus, Journal of Atmospheric and Solar-Terrestrial Physics, 75–76, 147–160, https://doi.org/10.1016/j.jastp.2011.11.008, 2012.
- 770 Mardia, K. V.: Statistics of Directional Data, Probability and Mathematical Statistics, Academic Press, London, New York, 1972.
  - Mass, C. F., Ovens, D., Westrick, K., and Colle, B. A.: DOES INCREASING HORIZONTAL RESOLUTION PRODUCE MORE SKILL-FUL FORECASTS?, 2002.
  - Mateus, P., Mendes, V. B., and Pires, C. A. L.: Global Empirical Models for Tropopause Height Determination, Remote Sensing, 14, 4303, https://doi.org/10.3390/rs14174303, 2022.
- Mellor, G. L. and Yamada, T.: A Hierarchy of Turbulence Closure Models for Planetary Boundary Layers, Journal of the Atmospheric Sciences, 31, 1791–1806, https://doi.org/10.1175/1520-0469(1974)031<1791:AHOTCM>2.0.CO;2, 1974.
  - Membrive, O., Crevoisier, C., Sweeney, C., Danis, F., Hertzog, A., Engel, A., Bönisch, H., and Picon, L.: AirCore-HR: A High-Resolution Column Sampling to Enhance the Vertical Description of CH<sub>4</sub> and CO<sub>2</sub>, Atmospheric Measurement Techniques, 10, 2163–2181, https://doi.org/10.5194/amt-10-2163-2017, 2017.
- 780 Meteomodem: M20 Meteosonde, 2020.
  - Miller, C., Fernández-Prieto, D., Bartsch, A., Fix, A., and Tamminen, J.: Arctic Methane and Permafrost Challenge (AMPAC), 2021.
  - Miner, K. R., Turetsky, M. R., Malina, E., Bartsch, A., Tamminen, J., McGuire, A. D., Fix, A., Sweeney, C., Elder, C. D., and Miller, C. E.: Permafrost Carbon Emissions in a Changing Arctic, Nature Reviews Earth & Environment, 3, 55–67, https://doi.org/10.1038/s43017-021-00230-3, 2022.
- Nakanishi, M. and Niino, H.: Development of an Improved Turbulence Closure Model for the Atmospheric Boundary Layer, Journal of the Meteorological Society of Japan. Ser. II, 87, 895–912, https://doi.org/10.2151/jmsj.87.895, 2009.
  - NCAR: Namelist.Wps: Best Practices, https://www2.mmm.ucar.edu/wrf/users/namelist\_best\_prac\_wps.html, 2024.
  - Olivier, J. and Janssens-Maenhout, G.: CO2 Emissions from Fuel Combustion, 2012 Edition, in: IEA CO2 Report 2012, Part III, Greenhouse-Gas Emissions, OECD Publishing, Paris, 2012.

- Ostler, A., Sussmann, R., Patra, P. K., Houweling, S., De Bruine, M., Stiller, G. P., Haenel, F. J., Plieninger, J., Bousquet, P., Yin, Y., Saunois, M., Walker, K. A., Deutscher, N. M., Griffith, D. W. T., Blumenstock, T., Hase, F., Warneke, T., Wang, Z., Kivi, R., and Robinson, J.: Evaluation of Column-Averaged Methane in Models and TCCON with a Focus on the Stratosphere, Atmospheric Measurement Techniques, 9, 4843–4859, https://doi.org/10.5194/amt-9-4843-2016, 2016.
- Patra, P. K., Houweling, S., Krol, M., Bousquet, P., Belikov, D., Bergmann, D., Bian, H., Cameron-Smith, P., Chipperfield, M. P., Corbin,
  K., Fortems-Cheiney, A., Fraser, A., Gloor, E., Hess, P., Ito, A., Kawa, S. R., Law, R. M., Loh, Z., Maksyutov, S., Meng, L., Palmer,
  P. I., Prinn, R. G., Rigby, M., Saito, R., and Wilson, C.: TransCom Model Simulations of CH<sub>4</sub> and Related Species: Linking Transport,
  Surface Flux and Chemical Loss with CH<sub>4</sub> Variability in the Troposphere and Lower Stratosphere, Atmospheric Chemistry and Physics,
  11, 12813–12837, https://doi.org/10.5194/acp-11-12813-2011, 2011.
- Pattanayak, S. and Mohanty, U. C.: Development of Extended WRF Variational Data Assimilation System (WRFDA) for WRF Non-Hydrostatic Mesoscale Model, Journal of Earth System Science, 127, 48, https://doi.org/10.1007/s12040-018-0949-9, 2018.
  - Peng, S., Lin, X., Thompson, R. L., Xi, Y., Liu, G., Hauglustaine, D., Lan, X., Poulter, B., Ramonet, M., Saunois, M., Yin, Y., Zhang, Z., Zheng, B., and Ciais, P.: Wetland Emission and Atmospheric Sink Changes Explain Methane Growth in 2020, Nature, 612, 477–482, https://doi.org/10.1038/s41586-022-05447-w, 2022.
- Peuch, V.-H., Engelen, R., Rixen, M., Dee, D., Flemming, J., Suttie, M., Ades, M., Agustí-Panareda, A., Ananasso, C., Andersson, E.,
  Armstrong, D., Barré, J., Bousserez, N., Dominguez, J. J., Garrigues, S., Inness, A., Jones, L., Kipling, Z., Letertre-Danczak, J., Parrington, M., Razinger, M., Ribas, R., Vermoote, S., Yang, X., Simmons, A., de Marcilla, J. G., and Thépaut, J.-N.: The Copernicus Atmosphere Monitoring Service: From Research to Operations, Bulletin of the American Meteorological Society, 103, E2650–E2668, https://doi.org/10.1175/BAMS-D-21-0314.1, 2022.
  - Picarro: Cavity Ring-Down Spectroscopy (CRDS) Picarro, https://www.picarro.com/company/technology/crds, 2008.
- Rantanen, M., Karpechko, A. Y., Lipponen, A., Nordling, K., Hyvärinen, O., Ruosteenoja, K., Vihma, T., and Laaksonen, A.: The Arctic Has Warmed Nearly Four Times Faster than the Globe since 1979, Communications Earth & Environment, 3, 1–10, https://doi.org/10.1038/s43247-022-00498-3, 2022.
  - Re3data.Org: HALO Database, https://doi.org/10.17616/R39Q0T, 2016.
- Rinne, J., Tuittila, E.-S., Peltola, O., Li, X., Raivonen, M., Alekseychik, P., Haapanala, S., Pihlatie, M., Aurela, M., Mammarella, I., and
  Vesala, T.: Temporal Variation of Ecosystem Scale Methane Emission From a Boreal Fen in Relation to Temperature, Water Table Position, and Carbon Dioxide Fluxes, Global Biogeochemical Cycles, 32, 1087–1106, https://doi.org/10.1029/2017GB005747, 2018.
  - Rio, C. and Hourdin, F.: A Thermal Plume Model for the Convective Boundary Layer: Representation of Cumulus Clouds, Journal of the Atmospheric Sciences, 65, 407–425, https://doi.org/10.1175/2007JAS2256.1, 2008.
- Saunois, M., Stavert, A. R., Poulter, B., Bousquet, P., Canadell, J. G., Jackson, R. B., Raymond, P. A., Dlugokencky, E. J., Houweling, S.,
  Patra, P. K., Ciais, P., Arora, V. K., Bastviken, D., Bergamaschi, P., Blake, D. R., Brailsford, G., Bruhwiler, L., Carlson, K. M., Carrol, M., Castaldi, S., Chandra, N., Crevoisier, C., Crill, P. M., Covey, K., Curry, C. L., Etiope, G., Frankenberg, C., Gedney, N., Hegglin, M. I., Höglund-Isaksson, L., Hugelius, G., Ishizawa, M., Ito, A., Janssens-Maenhout, G., Jensen, K. M., Joos, F., Kleinen, T., Krummel, P. B., Langenfelds, R. L., Laruelle, G. G., Liu, L., Machida, T., Maksyutov, S., McDonald, K. C., McNorton, J., Miller, P. A., Melton, J. R., Morino, I., Müller, J., Murguia-Flores, F., Naik, V., Niwa, Y., Noce, S., O'Doherty, S., Parker, R. J., Peng, C., Peng, S., Peters, G. P.,
- Prigent, C., Prinn, R., Ramonet, M., Regnier, P., Riley, W. J., Rosentreter, J. A., Segers, A., Simpson, I. J., Shi, H., Smith, S. J., Steele, L. P., Thornton, B. F., Tian, H., Tohjima, Y., Tubiello, F. N., Tsuruta, A., Viovy, N., Voulgarakis, A., Weber, T. S., van Weele, M., van der Werf, G. R., Weiss, R. F., Worthy, D., Wunch, D., Yin, Y., Yoshida, Y., Zhang, W., Zhang, Z., Zhao, Y., Zheng, B., Zhu, Q., Zhu, Q., and Zhuang,

- Q.: The Global Methane Budget 2000–2017, Earth System Science Data, 12, 1561–1623, https://doi.org/10.5194/essd-12-1561-2020, 2020.
- 830 Schuh, A. E., Jacobson, A. R., Basu, S., Weir, B., Baker, D., Bowman, K., Chevallier, F., Crowell, S., Davis, K. J., Deng, F., Denning, S., Feng, L., Jones, D., Liu, J., and Palmer, P. I.: Quantifying the Impact of Atmospheric Transport Uncertainty on CO2 Surface Flux Estimates, Global Biogeochemical Cycles, 33, 484–500, https://doi.org/10.1029/2018GB006086, 2019.
  - Segers, A.: Contribution to Documentation of Products and Services as Provided within the Scope of This Contract 2023 Part CH4, Tech. rep., Copernicus Atmosphere Monitoring Service, 2023.
- 835 Skamarock, C., Klemp, B., Dudhia, J., Gill, O., Barker, D., Duda, G., Huang, X.-y., Wang, W., and Powers, G.: A Description of the Advanced Research WRF Version 3, https://doi.org/10.5065/D68S4MVH, 2008.
  - Stohl, A.: Intercontinental Transport of Air Pollution, The Handbook of Environmental Chemistry, Springer Berlin, Heidelberg, 2004.
  - Sweeney, C., Chatterjee, A., Wolter, S., McKain, K., Bogue, R., Conley, S., Newberger, T., Hu, L., Ott, L., Poulter, B., Schifferl, L., Weir, B., Zhang, Z., and Miller, C. E.: Using Atmospheric Trace Gas Vertical Profiles to Evaluate Model Fluxes: A Case Study of Arctic-CAP Observations and GEOS Simulations for the ABoVE Domain, Atmospheric Chemistry and Physics, 22, 6347–6364, https://doi.org/10.5194/acp-22-6347-2022, 2022.
  - Tans, P. P.: System and Method for Providing Vertical Profile Measurements of Atmospheric Gases, 2009.
  - Taylor, K. E.: Summarizing Multiple Aspects of Model Performance in a Single Diagram, Journal of Geophysical Research: Atmospheres, 106, 7183–7192, https://doi.org/10.1029/2000JD900719, 2001.
- Tewari, M.: Implementation and Verification of the Unified Noah Land Surface Model in the WRF Model, in: 84th American Meteorological Society (AMS) Annual Meeting, 2004.
  - Thanwerdas, J., Saunois, M., Pison, I., Hauglustaine, D., Berchet, A., Baier, B., Sweeney, C., and Bousquet, P.: How Do Cl Concentrations Matter for the Simulation of CH<sub>4</sub> and  $\delta^{13}$ C(CH<sub>4</sub>) and Estimation of the CH<sub>4</sub> Budget through Atmospheric Inversions?, Atmospheric Chemistry and Physics, 22, 15 489–15 508, https://doi.org/10.5194/acp-22-15489-2022, 2022.
- Thompson, R. L., Patra, P. K., Ishijima, K., Saikawa, E., Corazza, M., Karstens, U., Wilson, C., Bergamaschi, P., Dlugokencky, E., Sweeney, C., Prinn, R. G., Weiss, R. F., O'Doherty, S., Fraser, P. J., Steele, L. P., Krummel, P. B., Saunois, M., Chipperfield, M., and Bousquet, P.: TransCom N<sub>2</sub>O Model Inter-Comparison Part 1: Assessing the Influence of Transport and Surface Fluxes on Tropospheric N<sub>2</sub>O Variability, Atmospheric Chemistry and Physics, 14, 4349–4368, https://doi.org/10.5194/acp-14-4349-2014, 2014.
  - Tiedtke, M.: A Comprehensive Mass Flux Scheme for Cumulus Parameterization in Large-Scale Models, Monthly Weather Review, 117, 1779, https://doi.org/10.1175/1520-0493(1989)117<1779:ACMFSF>2.0.CO;2, 1989.
  - Verma, S., Marshall, J., Parrington, M., Agustí-Panareda, A., Massart, S., Chipperfield, M. P., Wilson, C., and Gerbig, C.: Extending Methane Profiles from Aircraft into the Stratosphere for Satellite Total Column Validation Using the ECMWF C-IFS and TOMCAT/SLIMCAT 3-D Model, Atmospheric Chemistry and Physics, 17, 6663–6678, https://doi.org/10.5194/acp-17-6663-2017, 2017.
  - Virtanen, P.: Scipy/Interpolate/Interpnd.Pyx, SciPy, 2010.

840

- Waletzko, E. J. and Mitsch, W. J.: Methane Emissions from Wetlands: An in Situ Side-by-Side Comparison of Two Static Accumulation Chamber Designs, Ecological Engineering, 72, 95–102, https://doi.org/10.1016/j.ecoleng.2013.09.008, 2014.
  - Walsh, J. E.: Intensified Warming of the Arctic: Causes and Impacts on Middle Latitudes, Global and Planetary Change, 117, 52–63, https://doi.org/10.1016/j.gloplacha.2014.03.003, 2014.
- Weber, T., Wiseman, N. A., and Kock, A.: Global Ocean Methane Emissions Dominated by Shallow Coastal Waters, Nature Communications, 10, 4584, https://doi.org/10.1038/s41467-019-12541-7, 2019.

- Williams, J. E., Boersma, K. F., Le Sager, P., and Verstraeten, W. W.: The High-Resolution Version of TM5-MP for Optimized Satellite Retrievals: Description and Validation, Geoscientific Model Development, 10, 721–750, https://doi.org/10.5194/gmd-10-721-2017, 2017. Willmott, C. J.: Some Comments on the Evaluation of Model Performance, 1982.
- Wittig, S., Berchet, A., Pison, I., Saunois, M., Thanwerdas, J., Martinez, A., Paris, J.-D., Machida, T., Sasakawa, M., Worthy, D. E. J., Lan, X., Thompson, R. L., Sollum, E., and Arshinov, M.: Estimating Methane Emissions in the Arctic Nations Using Surface Observations from 2008 to 2019, Atmospheric Chemistry and Physics, 23, 6457–6485, https://doi.org/10.5194/acp-23-6457-2023, 2023.
  - Xiong, X., Barnet, C., Maddy, E., Wofsy, S., Chen, L., Karion, A., and Sweeney, C.: Detection of Methane Depletion Associated with Stratospheric Intrusion by Atmospheric Infrared Sounder (AIRS), Geophysical Research Letters, 40, 2455–2459, https://doi.org/10.1002/grl.50476, 2013.
- Yu, L., Zhong, S., Vihma, T., and Sun, B.: Attribution of Late Summer Early Autumn Arctic Sea Ice Decline in Recent Decades, npj Climate and Atmospheric Science, 4, 1–14, https://doi.org/10.1038/s41612-020-00157-4, 2021.
  - Zhang, Z., Poulter, B., Feldman, A. F., Ying, Q., Ciais, P., Peng, S., and Li, X.: Recent Intensification of Wetland Methane Feedback, Nature Climate Change, pp. 1–4, https://doi.org/10.1038/s41558-023-01629-0, 2023.
- Zheng, B., Ciais, P., Chevallier, F., Yang, H., Canadell, J. G., Chen, Y., van der Velde, I. R., Aben, I., Chuvieco, E., Davis, S. J., Deeter, M.,
  Hong, C., Kong, Y., Li, H., Li, H., Lin, X., He, K., and Zhang, Q.: Record-High CO2 Emissions from Boreal Fires in 2021, Science, 379,
  912–917, https://doi.org/10.1126/science.ade0805, 2023.